

# POLITECNICO DI TORINO

Master Degree in Nanotechnologies for ICTs



Master Degree Thesis

## Computer-aided design of grating VCSELs emitting circularly-polarized light

Supervisors

Dr. Alberto Tibaldi

Dr. Pierluigi Debernardi

Mr. Valerio Torrelli

Mr. Martino d'Alessandro

Candidate

RENATA DE GENNARO

31 October 2024



## Abstract

Vertical-cavity surface-emitting lasers (VCSELs) have become widely adopted in automotive systems, sensors, smartphones, short- and long- range communications. However, emerging applications such as polarization LIDARs (P-LIDARs), atomic clocks, and atomic magnetometers demand a stable, circular polarization of the lasing beam. This thesis seeks to explore possible designs for circularly-polarized (CP) VCSELs and to identify the key parameters that most significantly impact on CP performance.

In this thesis, CP VCSELs have been analysed by means of our in-house VCSEL ELectroMagnetic Suite (VELMS), serving as optical mode solver of Maxwell's equations, based on the mathematical framework of coupled mode theory. In particular, this thesis is focused on engineering optical anisotropies in VCSELs, specifically on investigating the impact of their orientation on the polarization features of the emitted light. Specifically, the electro-optic and elasto-optic effects, single and double sub-wavelength gratings have been considered either independently or in combination, aiming to determine which configuration will ultimately produce CP. Anisotropies have been incorporated into the model by extending the 1D version of VELMS, now accounting for the vectorial components of the optical field and able to extract polarization features.

The interplay between misaligned anisotropies is pivotal for CP; in this view, tilted sub-wavelength gratings play a key role. In the model, such tilted gratings have been analysed with different models, either by treating them as a homogeneous anisotropic medium described in terms of polarization-dependent effective indices, or by rigorous coupled wave analysis (RCWA). The output polarization is described by the Stokes parameters, with particular emphasis on  $S_3$ . Indeed,  $S_3 \pm 1$  represent fully CP light, either clockwise or counterclockwise.

The first structure analyzed is a single-grating VCSEL, with electro and elasto-optic effects oriented along the VCSEL's crystalline axis and with the grating at the outcoupling facet rotated with respect to them. This approach represents a slight modification of the state-of-the-art technology for achieving linear polarization, obtained by simply rotating the grating. When optimized in terms of technological parameters, specifically grating thickness and rotation angle, this configuration can produce CP. However, this solution could be strongly affected by unwanted technological factors, such as unwanted strain, impacting on the elasto-optic effect,

eventually degrading the CP output to elliptically polarized light.

Aiming at a more robust implementation, a more complex design has been proposed, where decoupled anisotropies are induced by multiple gratings. Specifically, a double grating structure with a spacer in the middle has been investigated. In this design, both gratings are placed at the VCSEL outcoupling facet. The lower grating, in contact with the top distributed Bragg reflector (DBR), is aligned with the crystalline axes, while the upper grating, exposed to air, is tilted. By carefully employing for simulations the parameters of reasonable materials, obtained by processes compatible with standard VCSEL technology, promising results have been obtained. Particularly, employing a sol-gel of  $\text{TiO}_2$  for both the spacer and the upper grating, and considering reasonable thermal curing, it is possible to obtain a refractive index of 2. A value of  $S_3 > 0.99$  has been achieved for a structure where the upper grating has a thickness of  $60 \div 70$  nm, with the spacer thickness of 100 nm, yet featuring a periodic behavior. A critical condition for this structure is that the period of the lower grating must be smaller than that of the upper one. The upper grating exhibits optimal performance when rotated at  $\theta = 45^\circ$ , or at least within the range  $\theta \in [40^\circ, 50^\circ]$ , with a period of  $\Lambda \in [200, 400]$  nm and a thickness of  $t \in [300, 400]$  nm.

The proposed structures are extremely promising for future technologically implementations in the view of more compact devices, not requiring external tools for polarization conversion.

## Thesis structure

The continuous requirements for circularly polarized emitting VCSELs for emerging technological and commercial applications in different fields, discussed into Chapter 2, are at the basis of this Master Thesis work. The main purpose is the study, the modeling and the characterization of a double-grating VCSEL with circular polarization emission, in order to propose an alternative way to obtain circular polarization with respect to the state of the art ones.

The thesis mainly contains a first part with the description of the mathematical model used and the physics at the basis of the VCSELs' working principles. Then, a single grating VCSEL structure is analysed in which different aspects are highlighted, in particular, the strain and the elettro-optic effect and the device response. The core of the thesis work is the analysis of a double-grating structure for the circular polarization output light. The proposed structure is analysed firstly by the technological point of view in order to understand what are the crucial and sensitive parameters that must be finely engineered. Subsequently, the results of the modelling simulations are reported to demonstrate the concrete potential of this structure.

# Table of Contents

Thesis structure . . . . .	iii
<b>List of Figures</b>	<b>III</b>
<b>1 Introduction and historical framework</b>	<b>1</b>
1.1 Semiconductor laser diodes working principles . . . . .	2
1.2 Diode lasers: EEL and VCSELs comparison . . . . .	3
<b>2 Applications of circularly polarized light</b>	<b>7</b>
2.1 Atomic clocks . . . . .	8
2.2 Atomic magnetometers . . . . .	10
<b>3 VCSELs optical modelling</b>	<b>13</b>
3.1 Coupled Mode Theory applied to VCSELs . . . . .	13
3.2 Vectorial VELMS 1D: generalization of the transmission matrix of a layer . . . . .	21
3.2.1 Mathematical description of anisotropies . . . . .	21
3.2.2 4x4 eigenvalue problem . . . . .	22
3.3 Figures of merit . . . . .	24
<b>4 Grating optical models</b>	<b>25</b>
4.1 Optical classification of crystals . . . . .	26
4.2 Born and Wolf model . . . . .	27
4.3 Grating definition . . . . .	29
4.4 Rigorous Coupled Wave Analysis - RCWA . . . . .	31
4.5 Homogenization model . . . . .	32
4.6 Limits of the homogenization model . . . . .	34
<b>5 Design strategies for circular polarization emission</b>	<b>36</b>
5.1 Poincarè sphere and Stokes parameters . . . . .	39

<b>6</b>	<b>Modeling results</b>	<b>42</b>
6.1	Single grating structure . . . . .	42
6.1.1	Analysis on rotated and non-rotated grating . . . . .	42
6.1.2	Elasto- and electro-optic effects: theoretical explanation . . .	44
6.1.3	Elasto-optic effects on rotated and non-rotated grating . . .	47
6.1.4	Electro-optic effects on rotated and non-rotated grating . . .	49
6.2	Double grating structure . . . . .	53
6.3	Titanium dioxide $\text{TiO}_2$ sol-gel processes . . . . .	54
6.4	Studies and technological implementations . . . . .	57
6.5	1D modelling results . . . . .	58
<b>7</b>	<b>Final considerations and future works</b>	<b>62</b>
	<b>Bibliography</b>	<b>64</b>

# List of Figures

1.1	Sketch of the stimulated emission principle . . . . .	3
1.2	EEL and VCSELs different light emission. . . . .	3
1.3	Cross-section of a VCSEL . . . . .	4
1.4	1D refractive index profile VCSEL, evolution along the z-axis of the refractive index. Starting from the substrate ( $n = 3.6$ ) and exiting in the air ( $n = 1$ ), then the DBRs have high refractive index $n_H = 3.5$ , low refractive index $n_L = 3$ . Conventionally the reference $z = 0$ is placed at the outcoupling facet, while positive $z$ coordinates go deeper into the device. . . . .	6
2.1	Atomic clocks schematic setup elements. . . . .	9
2.2	CPT ground state splitting scheme for Cs and Rb. . . . .	9
2.3	Zeeman energy levels splitting scheme for Rb. . . . .	10
3.1	VENUS main solver and their relation. . . . .	14
3.2	Simplified profile of the VCSEL structure described in terms of thicknesses and refractive index of each layer. The upper figure is a zoom of the red region to emphasise the presence of the cavity and the active region. . . . .	15
3.3	Simplified profile of the VCSEL structure within a reference medium. . . . .	16
3.4	2x2 transmission matrix of the structure, highlighting the forward and backward components of the field. . . . .	16
3.5	$\underline{T}^0$ and $\underline{T}^\gamma$ components. . . . .	19
3.6	Dispersion curves for the VCSEL structure. . . . .	20
3.7	Generalization of 4x4 matrix with its components. . . . .	22
4.1	Birefringence mechanism of crystals. . . . .	27
4.2	Relevant quantities for the model description. . . . .	28
4.3	Born-Wolf refractive index plot in function of duty-cycle. . . . .	30
4.4	RCWA schematic model. . . . .	31
4.5	Grating structure under analysis . . . . .	34



4.6	Homogenization and Born and Wolf models comparison . . . . .	35
5.1	Schematic of a VCSEL with CTF and a CSTF [29]. . . . .	37
5.2	VCSEL schematic featuring a chiral meta-surface as the top reflector. The top-left inset shows a top view of the meta-surface unit cell, with the geometric parameters labeled [30]. . . . .	38
5.3	The left image shows the refractive index and standing wave profile of VCSEL structure; whereas the right image represents the schematics of the cavity [31]. . . . .	38
5.4	Poincaré sphere and relevant polarization points. . . . .	41
6.1	3D single grating structure (left), simplified sketch with relevant parameters . . . . .	42
6.2	1D refractive index profile of single grating VCSEL structure when $t=150$ nm. The value of the refractive index associate is the isotropic one evaluated as $n = \sqrt{\frac{\epsilon_{TM} + \epsilon_{TE}}{2}}$ . . . . .	43
6.3	$\Delta f$ and $\Delta g$ plot for different grating thicknesses with a grating rotating angle of $45^\circ$ . . . . .	44
6.4	Stokes parameters comparison for VCSEL structures with 0, 100, 300 nm thick gratings in function of the gratings' rotating angle. In all the three plots solid lines are associated to the lasing mode, whereas the dashed lines refer to the second order mode. Red lines identify $S_1$ , green lines $S_2$ and the blue ones $S_3$ . . . . .	45
6.5	Frequency and threshold gain spacing comparison of VCSELs struc- ture with 0nm, 150nm, 300nm thick gratings. In the case in which the grating is present, it has been chosen a rotating angle of $45^\circ$ . . .	48
6.6	$S_3$ comparison for a VCSEL with 150nm thick grating rotated or not.	49
6.7	$S_3$ comparison for VCSELs with different grating thicknesses. . . .	49
6.8	Refractive index profile and standing wave for a VCSEL structure with 147 nm thick grating rotated of $53^\circ$ . . . . .	50
6.9	Electric field profile associated respectively to the top DBR (left plot) and the bottom one (right plot). . . . .	51
6.10	Dielectric constant profile into the VCSEL structure by means of electro-optic anisotropy. . . . .	51
6.11	$S_3$ (right) and $\Delta g$ (left) maps, associated to the lasing mode, for different grating thickness and rotating angles. The dashed lines of the second figure emphasize modal jumps where $\Delta g = 0$ . . . . .	52
6.12	Linear polarizer output associated to the red marker point. . . . .	52
6.13	Analysis on different applied bias, demonstrating that CP not de- pends on it. Blue lines refer to lasing mode, red ones to the superior mode. . . . .	53

6.14	Double gratings VCSEL structure technological process steps. . . .	53
6.15	Refractive index plot in function of the value of the temperature treatment of the sol-gel. . . . .	56
6.16	3D double-grating VCSEL structure (left); simplified sketch with relevant paramters definition (right). . . . .	57
6.17	Refractive index profile of the double-grating 1D-VCSEL structure.	58
6.18	$S_3$ map of the lasing mode for different grating rotating angles. . . .	59
6.19	$S_3$ map of the lasing mode for different grating periods (right); $S_3$ comparison plot for $\Lambda = 200, 300, 400$ nm and different grating thicknesses (left). . . . .	59
6.20	$S_3$ lasing mode map for different grating periods and thicknesses. .	60
6.21	$S_3$ lasing mode map for different values of applied strain (left). $S_3$ map in function of the sol-gel refractive index parametric variation (right). . . . .	60



# Chapter 1

## Introduction and historical framework

VCSELs were proposed for the first time in 1977 by Kenichi Iga at the Tokyo Institute of Technology, laying the groundwork for the technology's development [1]. The motivations behind Iga's work rely on some important limitations of the well known Fabry-Perot edge-emitting semiconductor lasers (EEL), that can be summarized in the following three main ones, [2]:

- The fabrication of EEL involved manually cleaving wafers, cutting an epitaxially grown wafer along a specific crystal plane with the cavity length of few hundred microns. This process is unsuitable for mass production and hindering initial quality checks; additionally, characterizing the device was only possible after cleaving.
- Achieving a single-mode laser was challenging; simulations suggested to work on the cavity length that should be shorter than  $50\text{ }\mu\text{m}$ .
- Controlling the lasing frequency in multi-mode EEL proved difficult due to factors like imprecise cavity length control.

These limitations led to propose a fundamentally different approach: the laser cavity should be made vertical. Moreover, this design would utilize semiconductor or dielectric epitaxial layers, enabling fabrication through established semiconductor processes, eliminating the need for manual cleaving. In 1988, a significant breakthrough occurred when Koyama and Iga achieved the first continuous-wave operation of a VCSEL at room temperature demonstrating the potential of a GaAs-based VCSELs as practical engineered semiconductor lasers.

## 1.1 Semiconductor laser diodes working principles

It is essential to revisit the working principles of laser diodes, before delving into the general structure of VCSELs. Generally speaking, laser are devices that require an optical resonator that contains an active medium; its working principle exploits the stimulated emission (firstly theorized by Albert Einstein in 1917, [3]). Among the several kind of commercially available lasers, the attention is here focused on semiconductor laser diodes, whose active medium is a semiconductor material, that can emit light into a wide range of wavelengths, opportunely tuned.

In semiconductor materials, electrons in general occupy the valence band - VB (associated to lower energies, where  $E_v$  is the higher energy value associated with the valence band), but can also move into the conduction band - CB (associated to higher energies, where  $E_c$  is the lower energy value associated with the conduction band) if opportunely stimulated with a photon with an incident energy  $h\nu = E_c - E_v = E_g$ , leaving behind a hole, leading to the absorption phenomenon. This promoted electron may lose its energy and return back to the original energy state in two different ways: through spontaneous or stimulated emission. The first one, consider an electron that spontaneously, after a certain time, losing energy falls into an energy level with lower energy, not necessary the original one, emitting a photon whose energy is equal to energy difference between the two energy states. The second one, consider an electron already excited into the CB that is subjected to an incident photon with energy  $h\nu = E_c - E_v = E_g$  exactly equal to the energy difference between CB and VB. The electron will return to its original state in the VB losing energy in the form of another photon, thus at the end leading to two photons, with same phase and same amplitude of the original one, Figure 1.1. In order to obtain a sufficiently high degree of amplification, it is necessary that the majority of electrons must occupy the CB leading to the so called population inversion principle.

Involving into the description only two energy levels, it is not possible to obtain a population inversion. Whereas, in some materials it is possible to find the so called metastable energy levels with an energy slightly inferior with respect to the excited state, where electrons can fall from the excited state with a fast and radiationless decay and stay for a longer interval of time. This means that is possible to populate this metastable level, by means of optical pumping. Once the population inversion is reached, through spontaneous dis-excitation electrons can turn to their original state losing energy in the form of photons emitted in all the directions.

Placing the active material into a resonance chamber, this photons will start to go

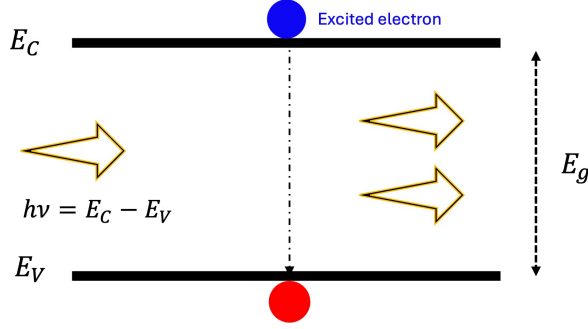


**Figure 1.1:** Sketch of the stimulated emission principle

bounce and back between the two mirrors progressively stimulated the photons production with the same energy leading to the definition of a cascade effect, in such a way all the photons will ultimately lead to the lasing beam with monochromatic, directional and coherent photons.

## 1.2 Diode lasers: EEL and VCSELs comparison

In the family of diode lasers, EEL - edge emitting lasers and VCSEL are the most common and used ones. As stated in Chapter 1, VCSELs were designed to overcome some EEL limitation; in this section their main differences will be analyzed. Among them, the more evident one is the direction from which the light is emitted: in EEL light is emitted from the edge of the device, parallel to the surface; while in VCSELs light is emitted perpendicular to the topmost surface, as it can be appreciated in Figure 1.2.

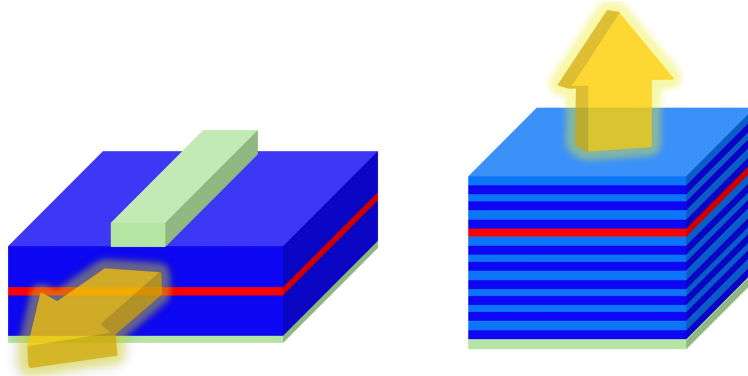


**Figure 1.2:** EEL and VCSELs different light emission.

From the technological point of view, an EEL has the optical cavity parallel to the

surface of wafer; then the wafer is cleaved at both ends and coated with mirrors. The endmost portion of the EEL has an high reflectivity coating with a reflectivity of almost 30% that allows the light to escape and not be reflected back into the cavity [4]. The emission of the light in EEL is achieved when the round trip (RT) condition is satisfied - Barkhausen stability criterion [5]

$$\beta \cdot 2L = m \cdot 2\pi, \quad (1.1)$$

where  $\beta$  is the propagation constant of the electric field,  $L$  is the cavity length, and  $m \in \mathbb{Z}$ . Among several cavity longitudinal modes, there is only one that satisfy the threshold condition  $RT = 1$ , the lasing mode. This condition can be splitted into two parts, one referred to the modulus  $|RT| = 1$  and the other linked to the phase  $\angle RT = 2m_l\pi$ , where  $m_l$  is the lasing modal number. Starting from the phase condition, recalling the expression of Equation 1.1 and considering that  $\beta = \frac{2\pi n_{eff}}{\lambda_m}$  ( $n_{eff}$  is the effective index) it is possible to reconstruct the expression of the lasing wavelength  $\lambda_l$  :

$$\lambda_l = \frac{2n_{eff}L}{m_l}. \quad (1.2)$$

Moreover, more complex cavity layouts are required when the laser single mode emission is required, using distributed Bragg reflectors (DBR) or distributed feed-back Bragg lasers (DFB) that allows to obtain a single longitudinal mode emission.

Concerning VCSELs on the other hand, a schematic cross section is reported in Figure 1.3. VCSELs designed for emission wavelengths in the 850 to 980 nm spectral range, have a short cavity length  $L_{cav} = \lambda/n$ , (where  $\lambda$  is the lasing wavelength and  $n$  is the effective refractive index of the cavity), thus in order to achieve an appreciable gain and to have low losses (so a reflectivity of the order of 99.5%) the geometry of the structure must be finely engineered.

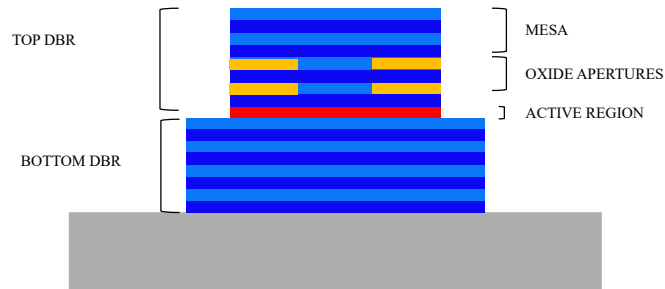


**Figure 1.3:** Cross-section of a VCSEL

The main building blocks, starting from the bottom and progressively going to the top, of such a laser are:

- Bottom DBR  $\rightarrow$  made out of a stack of an even number alternating high and low contrast layers, in order to achieve the maximum reflectivity in correspondence of a certain target wavelength. In order to satisfy this requirement, the corresponding thickness of each layer must satisfy the following relation:  $L = \lambda/(4n)$  where  $n$  is the corresponding refractive index (high or low). As previously stated, in order to achieve lasing, the mirror reflectivity must be of the order of 99% and even more. The parameter that is involved into the desired reflectivity is the difference in the refractive index of contiguous layers, with the purpose of creating an high refractive index contrast that is fundamental. Thus, the larger is the that difference, the lower is the number of mirror pairs necessary. For this reason that the choice of the kind of material used for VCSELs is crucial. Usually, a DBR is composed of Gallium Arsenide - Aluminum Gallium Arsenide (GaAs/AlGaAs) layers that are epitaxially grown using metalorganic vapour-phase epitaxy(MOVPE). [6].
- Active region  $\rightarrow$  composed of a stack of quantum wells (MQWs) 6-7 nm thick, is the region in which the stimulated emission occurs (as described in Section 2.1). The active region must be properly engineered in terms of its band gap since it has the aim of determine the material gain in function of several parameters, such as the temperature, the wavelength and the carrier's density.
- Oxide apertures  $\rightarrow$  they have the purpose to optically confine the field and to electrically confine the carriers, thus reducing the diameter of the structure with respect to the MESA. This can be performed by means of wet oxidation from the top such that only the layer of the top-DBR with a molar fraction of Aluminum of 0.97 – 0.98 starts to oxidaze. The problem is that having a wider aperture lead to the transversal multi-mode emission of the light, while in applications a single-mode emission is required. Thus, for this purpose, the oxide apertures discriminates where the light must be confined. In general, what is required is a perfect circular geometry of the oxide apertures, but since its diameter should be  $< 3\mu m$ , technological limitations lead to several troubles in its realization.
- Top DBR  $\rightarrow$  has the same technological composition of the bottom one, the main difference between the two is the number of the mirrors pairs used. In particular, the bottom DBR has more mirror pairs with respect to the top one. This because, the top-DBR has the role of permit the light emission; thus having less pairs of mirrors, the reflectivity is reduced into the cavity, favouring the light transmission and improving the optical efficiency.



The 1D profile of the VCSEL structure analysed in this work can be seen in Figure 1.4 where are also evident the two end of the device, respectively the substrate and the air. This is a simplified and ideal structure that can be analysed only by the optical point of view lacking of QWs and oxide aperture.

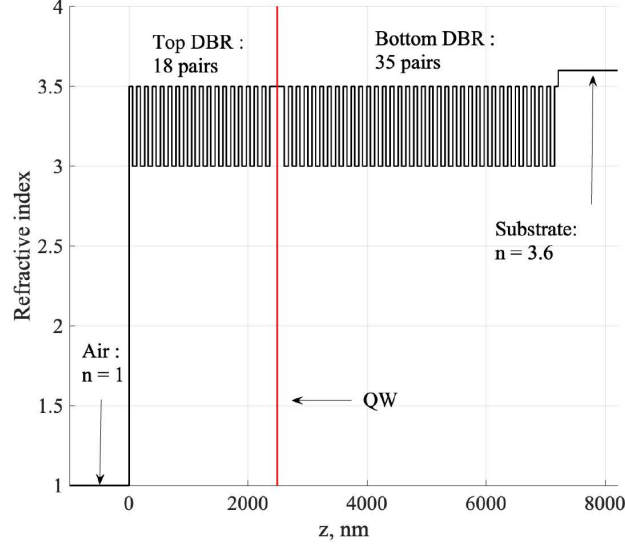


**Figure 1.4:** 1D refractive index profile VCSEL, evolution along the  $z$ -axis of the refractive index. Starting from the substrate ( $n = 3.6$ ) and exiting in the air ( $n = 1$ ), then the DBRs have high refractive index  $n_H = 3.5$ , low refractive index  $n_L = 3$ . Conventionally the reference  $z = 0$  is placed at the outcoupling facet, while positive  $z$  coordinates go deeper into the device.

## Chapter 2

# Applications of circularly polarized light

VCSELs were first commercialized by Honeywell in 1996 and have gained significant traction in recent decades, with their applications rapidly multiplying since the mid-1990s. Initially, they were employed in data communication, than by the mid-2010s, their applications had expanded to include sensors, printers, and even computer mouse pointers [7], [8]. While data communication and sensing remain the primary markets for VCSELs, with continued growth expected, these versatile lasers are making inroads into exciting new areas. These include 3D-sensing for facial recognition in smartphones, Laser Imaging Detection and Ranging (LIDAR), atomic clocks, atomic magnetometers and gyroscopes.

In particular, for applications such as atomic clocks, bio-sensing atomic magnetometers and LIDAR, circularly polarized emitting VCSELs (CP-VCSEL) are fundamental, because circular polarization is required to enforce selection rules on the optical transitions.

The first clues about polarized light emerged in 1669, but was Huygens in 1678 to mathematically explained this phenomenon [9]. Since than, polarized light has been used to describe reflection and scattering processes which are the foundations for the analysis of different surfaces and during the years several attempt have been performed in order to apply this concept to several applications.

This section focuses on understanding the requirements of CP - VCSELs for the mentioned applications. It aims to explain the significance of the numerous studies on CP - VCSELs and the relevance of this thesis work.

## 2.1 Atomic clocks

The scientist Isidor Rabi (Nobel Price in 1944) proposed for the first time the idea of an atomic clock [10], whose core concept lies in harnessing the oscillations of electromagnetic waves emitted by atomic transition of particular atoms at particular frequencies (cesium atoms at the beginning), rather than relying on mechanical or electrical oscillations of macroscopic physical systems. During the years the NBS-NIST institute proposed different atomic clocks up to the NIST-7 that was the first atomic clock in which the atomic transition of Cs atoms was induced by a laser source. The studies on this particular atomic clock converged into 1967 to the new definition of the second, the basic unit of measurement of time, as the numerical value of the frequency of the hyperfine transition of the unperturbed ground state of the cesium 133 atom, set at 9 192 631 770 Hz [11].

In time, atomic clocks have gained a widespread in many applications such as communication, navigation, computer networks and in the aerospace field requiring precise real-time measurements. New technologies have been implemented, especially using VCSELs. It is important to explore the physical theory at the basis on the atomic clocks in order to understand what is the role played by VCSELs.

Alkali metals like cesium (Cs) and rubidium (Rb) are involved in atomic clocks because their ground state transitions can be manipulated using Coherent Population Trapping (CPT) theory. These elements have transitions in the near-infrared (NIR) range, conveniently accessible by VCSELs. Specifically, the absorption lines of rubidium D1 at 795nm and cesium D1 at 852nm are particularly interesting for these applications [12].

A detailed description of the CPT method is provided in [13], however here some details are provided in view of our purpose.

Figure 2.1 shows the required setup of a CPT atomic clock: a 4.6 GHz microwave source is needed to drive the VCSEL (with a wavelength tuned around 850 nm - 852 nm for Cs and 795 nm for Rb). The VCSEL structure should include a grating (in the next chapters gratings will be deeply described), with the aim of ensure a linear polarized output beam. During the path, before reaching and excite the Cs or Rb vapour cell, the light beam encounter a quarter-wave plate (QWP), in such a way the polarization of the light turns to be circular. Finally, a photodiode is placed to measure the transmission of the VCSEL light.

CPT clocks rely on the precise excitation of two closely spaced energy levels in the alkali atoms. Due to the interaction between an electron's spin and the nucleus's spin (hyperfine interaction), the ground state splits into two sublevels for these elements. This splitting is specific for each element, with frequencies of 6.8 GHz

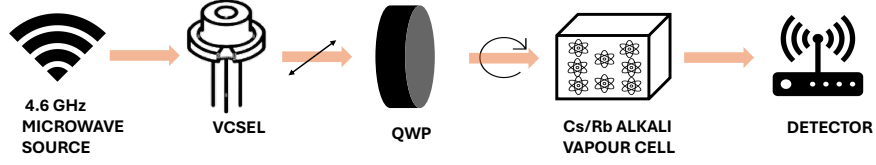


**Figure 2.1:** Atomic clocks schematic setup elements.

for Rb D1 and 9.2 GHz for Cs D1, independent on temperature or pressure. A simplified explanation scheme of the previous statement is depicted in Figure 2.2.

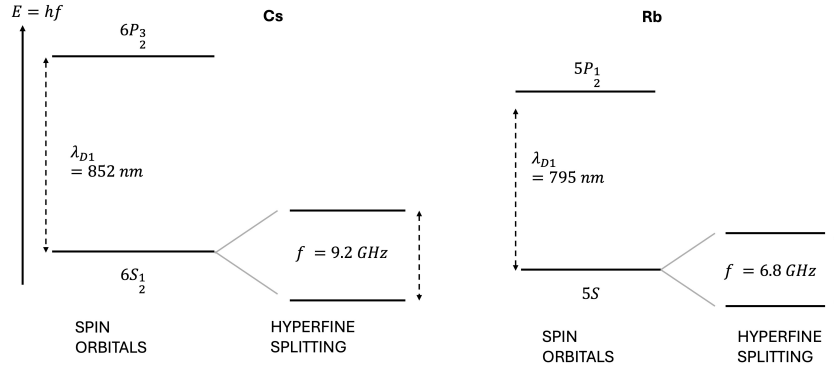


**Figure 2.2:** CPT ground state splitting scheme for Cs and Rb.

When these two closely spaced transitions are excited simultaneously with circularly polarized light with a modulation frequency equal to the ground state hyperfine splitting, an interesting phenomenon occurs. The gas cell, initially strongly absorbing light, becomes more transparent. This change in absorption is associated to the fact that a part of the Cs or Rb atoms are trapped in a coherent superposition of the two splitted sub-levels of the ground state that do not absorb light, known as dark-state, thus no energy transition occurs. This phenomenon makes the time measurements more stable and precise since the atomic clock is not so sensitive to external perturbations and fluctuations.

CP light is crucial for CPT, as linearly polarized light cannot excite the hyperfine-split levels due to symmetry constraints [13]. Therefore, a quarter-wave plate (QWP) is necessary to convert the linear polarization to circular polarization. However, achieving a single-mode, linearly polarized output for the QWP is challenging. As a potential solution, using a VCSEL that directly emits CP-light could overcome these technological limitations.

## 2.2 Atomic magnetometers

Many scientific fields such as geophysics, archeology, cosmo-physics and bio-physics require the measurements of very weak magnetic fields accessible using atomic magnetometers. The design of the atomic magnetometers, is similar to the one of the atomic clocks previously shown 2.1 without the presence of a microwave source; in the magnetometers setup we have a VCSEL that emits a linear polarized light that passes through a QWP in order to have a circular polarization light and a lens system that collimates the beam in order to be focused on an alkali vapour cell that is at the end detected by a photo-detector. Even in this application, the presence of QWP is essential to achieve CP, making the system structure bulky and expensive. Let's see why CP is a necessary requirement for the atomic magnetometers' working principle.

The difference between the atomic clocks and atomic magnetometers architectures rely in the physics at the basis, in particular, while atomic clocks are based on hyperfine splitting, atomic magnetometers are based on the Zeeman splitting of the atomic energy levels [13], shown in Figure 2.3.

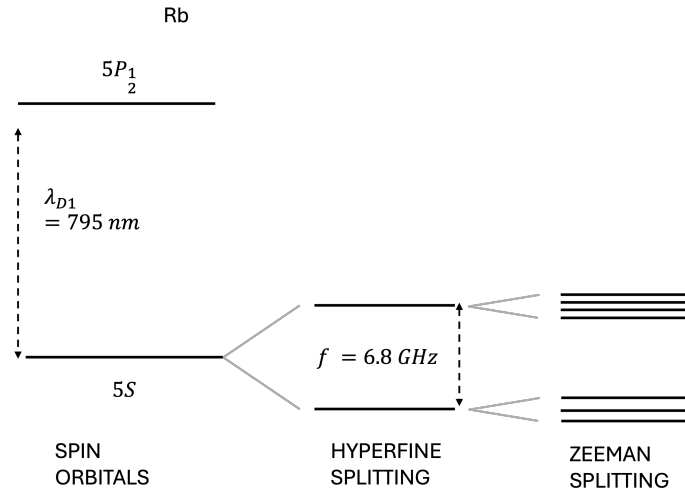


**Figure 2.3:** Zeeman energy levels splitting scheme for Rb.

An alkali-atoms cell (usually Rb) is optically pumped through a VCSEL that must be in resonance with a specific atomic transition (D1 for the Rb atoms at 6.8 GHz). When circularly polarized light interacts with the alkali metal vapor, it preferentially excites ground-state atoms, aligning their spins along the light direction. By carefully controlling this light interaction with the atoms, transitions

between an optically dark state (where light is not absorbed) and an absorbing state can be induced. The critical aspect lies in setting the oscillation frequency of the light to match the Zeeman splitting caused by the magnetic field. This resonance condition allows the magnetic field to influence the light absorption by the atomic vapor, which can be detected by measuring changes in the transmitted light intensity, [14].

Various configurations for chip-scale commercial atomic magnetometers exist and presented in [15] also deeply analyzing the physical theory at the basis, nevertheless, in this section the ones based on CPT are briefly described. In this approach, the magnetometer probes the hyperfine splitting within the ground state between specific Zeeman sub-levels. By measuring the response of the atomic ensemble to this manipulation, the magnetometer determines the magnetic flux density it experiences. For completeness, there are also chip-scale atomic magnetometer based on the spin-exchange relaxation-free (SERF) principle, that are the most studied and technologically advanced ones.

Magnetic fields generated by the human heart hold valuable information for medical diagnosis. Unlike electrical signals measured by ECGs, these magnetic signals are less affected by body tissues due to the body's nearly uniform magnetic permeability. This offers a more reliable way to detect biological activity within the heart. Combining both ECG and MCG (Magnetocardiography) can improve the diagnosis of cardiac arrhythmias and coronary artery disease. In this context, atomic magnetometers play a crucial role. Conventional atomic magnetometers may not be ideal for measuring cardiac magnetism due to their limitations in sensitivity. However, a breakthrough came in 2004 when Peter D. Schwindt's research group developed a chip-scale atomic magnetometer based on the CPT resonance principle specifically designed for medical applications. These technologies have seen continuous improvement over the years, as detailed in [14].

When it comes to light sources for bio-sensing applications in atomic magnetometers, VCSELs have emerged as the preferred choice over Distributed Feedback (DFB) lasers. While DFB lasers offer advantages like high power, narrow linewidth, low noise, and stability, their large size and high cost make them less suitable for mass production. VCSELs, on the other hand, are smaller and more cost-effective, making them the dominant light source in commercially available chip-scale magnetometers.

The development of nano-fabrication techniques has revolutionized atomic biosensors VCSELs base. This compatibility allows for the miniaturization of these devices into chip-scale formats, paving the way for a new era in bio-sensing applications. Compared to traditional light sources, VCSEL integration in atomic

magnetometers offers several compelling advantages. These include enhanced portability, improved cost-effectiveness, and greater potential for industrial-scale production. Additionally, advancements include the integration of meta-surfaces enables further size reduction while maintaining precise control over the wavefront and the polarization of the emitted light. Surface grating etching remains the most cost-effective and efficient method for controlling the mode and polarization of VCSELs even for bio-sensing magnetometers. However, emerging research explores also an alternative approach based on the integration of polarization splitting or metalens, which offer promising features for future VCSEL development, even if they are still at the embryonic level [16].

## Chapter 3

# VCSELs optical modelling

Modeling a fully 3D VCSEL requires advanced mathematical tools, since a circular geometry must be analysed and different physical phenomena - electrical, thermal and optical - are involved into the complete description of the VCSEL working principles.

Even though many model exist the one that has been chosen in this work is the VENUS model (Vcsel Electro-opto-thermal NUmerical Simulator)[17]. As the name suggests, the electrical, optical and thermal analysis are involved for a complete description of the device, in particular, each of them turn out important parameters that are required for the solution of the rate equations (RE) which are the main equations to be solved. Any comprehensive model should be composed of 4 building blocks, shown in Figure 3.1: the vectorial 3D optical solver - VCSEL ELectroMagnetic Suite (VELMS), the quantum well optical response, the quantum-corrected drift-diffusion solver and the heat solver; that are strictly connected and related. Nevertheless, in this work the attention has been focused on the electromagnetic analysis of the VCSEL, thus only the VELMS model has been employed.

### 3.1 Coupled Mode Theory applied to VCSELs

Coupled mode theory (CMT) is a mathematical tool that gained popularity in the field of optics. It allows to analyze how electromagnetic waves propagate and interact with various materials found in optical devices. Over time, researchers have developed different formalism within CMT to suit the specific needs of analyzing particular devices. A brief historical overview of this development can be found in [18].



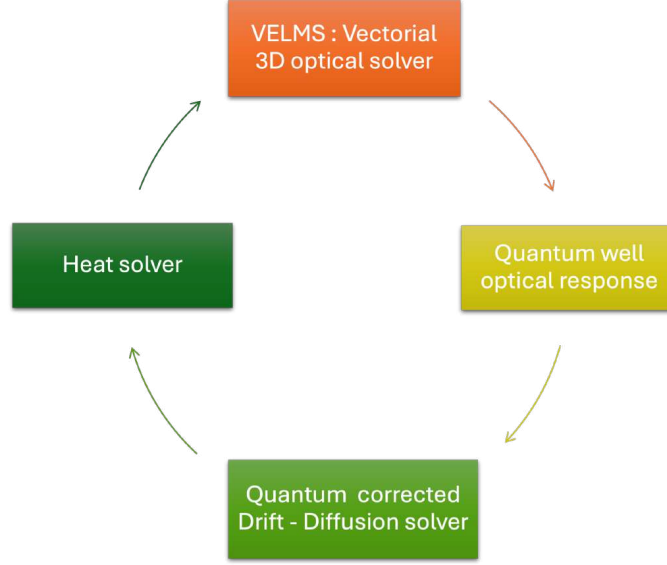


**Figure 3.1:** VENUS main solver and their relation.

For VCSEL application, the CMT formalism used has been proposed and analysed in depth in [19]. In this section, the main CMT requirements description is useful to have an overall view of the mathematics, moreover, these requirements are sufficient for the understanding of the Vectorial 1D - VELMS generalization. The mathematics discussed in this section is the one that is employed in our VELMS, used for all the analysis performed in this work.

Figure 3.6 shows a simple VCSEL structure, useful to understand the required ingredients for the solution of the problem.

The structure can be divided into three main parts, namely the bottom stack, the active region and the top stack in which each layer of these three regions is described in terms of refractive index  $n^i$  and thickness  $L^i$ . In particular:

- top stack  $\rightarrow$  takes into account, starting from topmost part and moving towards the bottom layer, the top DBR, half of the cavity thickness minus half of the active region thickness (red arrow in Figure 3.6). Going into details, the top DBR is described in terms of  $n_T^i = [n_H, n_L] \cdot N_T$  (where  $n_H$  and  $n_L$  are respectively the high and low refractive index of the mirrors) and  $L_T^i = [L_H, L_L] \cdot N_T$ , (where  $L_H = \frac{\lambda_t}{4n_H}$  and  $L_L = \frac{\lambda_t}{4n_L}$ , being  $\lambda_t$  the target wavelength of the lasing mode of the VCSEL under analysis fixed at 850 nm).  $N_T$  is the number of top pairs and  $i \in 1, \dots, N_T$ . The half of the cavity thickness is instead defined as:  $\frac{L_{cav}}{2} = \frac{\lambda_t}{2n_a}$  (with  $n_a$  the refractive index of the active region) and refractive index  $n_{cav}$ .

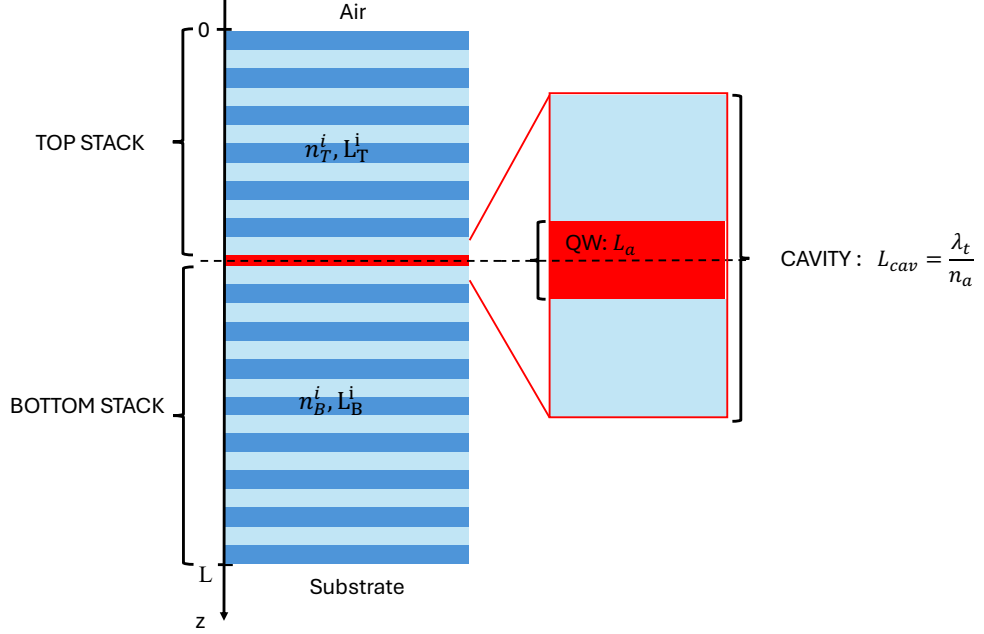


**Figure 3.2:** Simplified profile of the VCSEL structure described in terms of thicknesses and refractive index of each layer. The upper figure is a zoom of the red region to emphasise the presence of the cavity and the active region.

- active region  $\rightarrow$  described in terms of refractive index  $n_a$  and thickness  $L_a$
- bottom stack  $\rightarrow$  takes into account, progressively reaching the endmost layer, half of the cavity minus half of the active region thickness and the bottom DBR. All the mentioned quantities are described in the same way of what is done in the left stack.

Within the CMT formalism, each layer is assumed to be placed within a certain reference medium  $r$ , see Figure 3.3 ; focusing on the interval  $z \in [0^+, L^-]$ , it is possible to take into account the presence of a semi-infinite media through the expression of reflection coefficients:

$$\Gamma_T := \Gamma_{r \rightarrow n_T} = \frac{r - n_T}{r + n_T} \quad (3.1)$$

and

$$\Gamma_B := \Gamma_{r \rightarrow n_B} = \frac{r - n_B}{r + n_B}. \quad (3.2)$$

The transmission matrix of the entire structure is nothing but the product of the transmission matrix of the tree main blocks described before, that in this first case

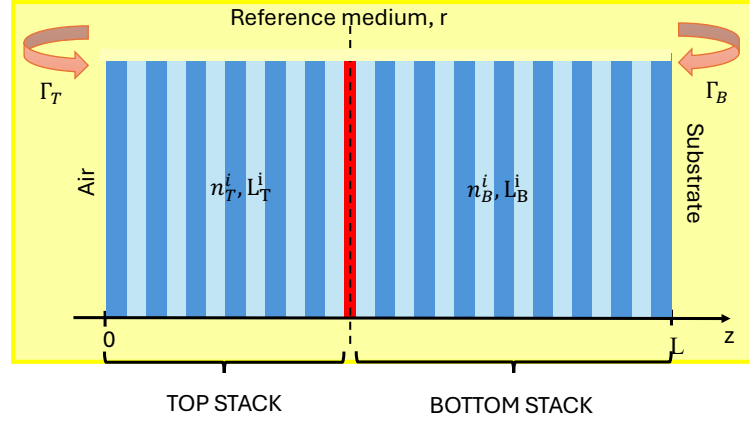


**Figure 3.3:** Simplified profile of the VCSEL structure within a reference medium.

is a 2x2 matrix (see Figure 3.4 where the forward and backward components of the electro-magnetic field are highlighted):

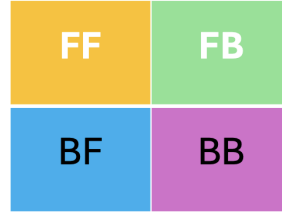


**Figure 3.4:** 2x2 transmission matrix of the structure, highlighting the forward and backward components of the field.

$$\underline{\underline{T}} = \prod_1^i \underline{\underline{T}}_i = \underline{\underline{T}}_T \underline{\underline{T}}_a \underline{\underline{T}}_B, \quad (3.3)$$

where

$$\underline{\underline{T}}_T = \prod_{i=1}^{N_T} \exp(\underline{\underline{M}}_i^T L_i^T) = \left( \underline{\underline{T}}_{n_i^T \rightarrow r} \begin{bmatrix} \exp(-j\beta n_i^T L_i^T) & 0 \\ 0 & \exp(+j\beta n_i^T L_i^T) \end{bmatrix} \underline{\underline{T}}_{r \rightarrow n_i^T} \right), \quad (3.4)$$

and

$$\underline{\underline{T}}_B = \prod_{i=1}^{N_B} \exp(\underline{\underline{M}}_i^B L_i^B) = \prod_{i=1}^{N_B} \left( \underline{\underline{T}}_{n_i^B \rightarrow r} \begin{bmatrix} \exp(-j\beta n_i^B L_i^B) & 0 \\ 0 & \exp(+j\beta n_i^B L_i^B) \end{bmatrix} \underline{\underline{T}}_{r \rightarrow n_i^B} \right), \quad (3.5)$$

being  $\underline{\underline{M}}_i^r$  and  $\underline{\underline{M}}_i^l$  the coupling matrix of each considered layer and  $\beta$  the propagation constant. The transmission matrix of the active region is

$$\underline{\underline{T}}_a = \exp\left(\underline{\underline{M}}_a^{s.e} La\right), \quad (3.6)$$

where

$$\underline{\underline{M}}_a^{s.e} La = -j \frac{\beta_r La}{2} \left( \begin{bmatrix} 2 & 0 \\ 0 & -2 \end{bmatrix} + \delta_a^{s.e} \begin{bmatrix} 1 & 1 \\ -1 & -1 \end{bmatrix} \right) \quad (3.7)$$

with

$$\delta_a^{s.e} = \frac{(n_a^{s.e})^2 - r^2}{r^2} \quad (3.8)$$

and  $\beta_r$  the propagation constant within the reference medium. Once the cavity support a lasing mode, the quantum well cannot be described any more simply by  $n_a$ , but the refractive index must be modified by properly taking into account the stimulated emission, so that:

$$n_a^{s.e} = n_a + \Delta \tilde{n}_a \in \mathbb{C}. \quad (3.9)$$

In a transversely invariant structure the coefficients of the modes propagating forward (F) and backward (B)  $|a(z)\rangle = [a^+ a^-]^T$  the Barkhausen stability criterion can be derived using the following relations:

$$\begin{cases} a^+(0^+) = a^-(0^+) \Gamma_l \\ a^-(L^-) = a^+(L^+) \Gamma_r \end{cases} \quad (3.10)$$

$$\begin{cases} a^+(L^-) = T_{11} a^+(0^+) + T_{12} a^-(0^+) \\ a^-(L^-) = T_{21} a^+(0^+) + T_{22} a^-(0^+) \end{cases} \quad (3.11)$$

These are four equations with 4 unknowns that can be rearranged once the attention is focused on  $a^-(0^+) = a_b$  associated to the back-scattered field, so that:

$$a^-(L^-) = \Gamma_r a^+(L^+) = \Gamma_r T_{11} a^+(0^+) + \Gamma_r T_{12} a_b. \quad (3.12)$$

Equating the second Eq 3.11 and Eq 3.12 yields to:

$$T_{21} a^+(0^+) + T_{22} a_b = \Gamma_r T_{11} a^+(0^+) + \Gamma_r T_{12} a_b. \quad (3.13)$$

Replacing the first Eq 3.10:

$$\begin{aligned} T_{21} a^-(0^+) \Gamma_l + T_{22} a_b &= \Gamma_r T_{11} a^-(0^+) \Gamma_l + \Gamma_r T_{12} a_b \\ \implies T_{21} a_b \Gamma_l + T_{22} a_b &= \Gamma_r T_{11} a_b \Gamma_l + \Gamma_r T_{12} a_b. \end{aligned} \quad (3.14)$$

Finally, this yields to the Barkhausen criterion definition as:

$$\begin{aligned} a_b (\Gamma_r T_{11} \Gamma_l + \Gamma_r T_{12} - \Gamma_l T_{21} - T_{22}) &= 0 \\ \implies \Gamma_r T_{11} \Gamma_l + \Gamma_r T_{12} - \Gamma_l T_{21} - T_{22} &= 0, \end{aligned} \quad (3.15)$$

once the non-trivial solution is considered ( $a_b \neq 0$ ). This last equation can be used in order to define the value of the refractive index of the QW once there are lasing modes to be supported. In particular, being

$$n_a^{s.e} := n_a + \Delta \tilde{n}_a := n_a + \Delta n + j \frac{g_{field}}{k} \quad (3.16)$$

$\Delta n$  is the real part of refractive index variation of the QW and  $g_{field}$  is the field gain to be determined, so that it is possible to write:

$$\delta_a^{s.e} := \frac{(n_a + \Delta \tilde{n}_a)^2 - r^2}{r^2} \simeq \frac{n_a^2 - r^2}{r^2} + \frac{2n_a \Delta \tilde{n}_a}{r^2} := \delta_a^0 + \delta_a^\gamma \quad (3.17)$$

considering  $|\Delta \tilde{n}_a| \ll n_a$  so that the second order contribute can be neglected. Equation 3.7 can be rewritten as:

$$\begin{aligned} \exp(\underline{\underline{M}}_a^{s.e} L_a) &= \exp \left\{ -j \frac{\beta_r L_a}{2} \left( \begin{bmatrix} 2 & 0 \\ 0 & -2 \end{bmatrix} + \delta_a^{s.e} \begin{bmatrix} 1 & 1 \\ -1 & -1 \end{bmatrix} \right) \right\} \\ \exp \left\{ -j \frac{\beta_r L_a}{2} \frac{2n_a \Delta \tilde{n}_a}{r^2} \begin{bmatrix} 1 & 1 \\ -1 & -1 \end{bmatrix} \right\} &\implies \underline{\underline{T}}_a^0 \exp \left( \gamma_{field} \begin{bmatrix} 1 & 1 \\ -1 & -1 \end{bmatrix} \right) \end{aligned} \quad (3.18)$$

where  $\underline{\underline{T}}_a^0$  is the transmission matrix associated to the active region if it was described only by  $n_a$ . In order to find the cold cavity modes (the cold cavity approximation takes into account the fact that the the value of the real part of the refractive index is not modified by any temperature or carriers effects), it is necessary to impose  $\Delta n = 0$  so that the field gain can be described in terms of threshold gain,  $g_{field} = g_{field}^{th}$ . The explicit expression of  $\gamma_{field}$  can be written as:

$$\gamma_{field} = -jkr \frac{L_s}{2} \frac{2n_a}{r^2} j \frac{g_{field}^{th}}{k} = \frac{n_a L_a g_{field}^{th}}{r}. \quad (3.19)$$

Expanding eq 3.18 using Taylor expansion yields to:

$$\exp(\underline{\underline{M}}_a^{s.e} L_a) \simeq \underline{\underline{T}}_a^0 \left( \underline{\underline{I}} + \gamma_{field} \begin{bmatrix} 1 & 1 \\ -1 & -1 \end{bmatrix} \right) = \underline{\underline{T}}_a^0 + \gamma_{field} \underline{\underline{T}}_a^0 \begin{bmatrix} 1 & 1 \\ -1 & -1 \end{bmatrix}. \quad (3.20)$$

Usually in the VCSEL analysis the interesting parameter is the threshold gain  $g_{th}$  that is related to the field threshold gain through the relation  $g_{th} = 2g_{field}^{th}$ , thus rewriting 3.19 in terms of  $g_{th}$ , so that  $\gamma = 2\gamma_{field}$ , eq. 3.20 can be rewritten as:

$$\exp\left(\underline{\underline{M}}_a^{s.e.} L_a\right) \simeq \underline{\underline{T}}_a^0 + \frac{1}{2}\gamma \underline{\underline{T}}_a^0 \begin{bmatrix} 1 & 1 \\ -1 & -1 \end{bmatrix} \quad (3.21)$$

Finally, eq. 3.3 assume the form of:

$$\underline{\underline{T}} = \underline{\underline{T}}_T \underline{\underline{T}}_a \underline{\underline{T}}_B = \underline{\underline{T}}_T \left( \underline{\underline{T}}_a^0 + \frac{1}{2}\gamma \underline{\underline{T}}_a^0 \begin{bmatrix} 1 & 1 \\ -1 & -1 \end{bmatrix} \right) \underline{\underline{T}}_B = \underline{\underline{T}}^0 + \gamma \underline{\underline{T}}^\gamma, \quad (3.22)$$

where  $\underline{\underline{T}}^0$  is the transmission matrix of the VCSEL embedded into the reference medium without modifying the QW refractive index, while  $\underline{\underline{T}}^\gamma$  is the transmission matrix depending on the QW index variation. Once again, they are 2x2 matrices, 3.5

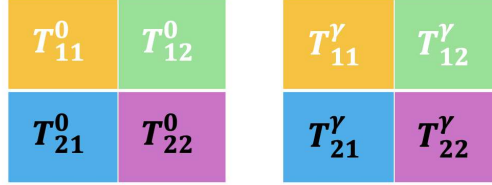


**Figure 3.5:**  $\underline{\underline{T}}^0$  and  $\underline{\underline{T}}^\gamma$  components.

Finally, the Barkhausen criterion can be written as:

$$R^0 + \gamma R^\gamma = 0 \quad (3.23)$$

where

$$R^0 := \Gamma_l \Gamma_r T_{11}^0 + \Gamma_r T_{12}^0 - \Gamma_l T_{21}^0 - T_{22}^0 \quad (3.24)$$

$$R^\gamma := \Gamma_l \Gamma_r T_{11}^\gamma + \Gamma_r T_{12}^\gamma - \Gamma_l T_{21}^\gamma - T_{22}^\gamma \quad (3.25)$$

Defining

$$C := -\frac{R^0}{R^\gamma} \quad (3.26)$$

Combining 3.24, 3.26 and  $\gamma = 2\gamma_{field}$  one gets:

$$\gamma = -\frac{R^0}{R^\gamma} \implies -2jk\Delta\tilde{n}_a \frac{n_a L_a}{r} = C(\lambda)$$

$$\implies -2jk\Delta\tilde{n}_a = \frac{r}{n_a L_a} C(\lambda), \quad (3.27)$$

recalling the expression of  $\Delta\tilde{n}_a$ , see 3.16 and substitution, it is possible to write:

$$\begin{aligned} -2jk \left( \Delta n_a + j \frac{g_{field}}{h} \right) &= \frac{r}{n_a L_a} C(\lambda) \implies -2jk\Delta n_a + 2g_{field} = \frac{r}{n_a L_a} C(\lambda). \\ \implies -2jk\Delta n_a + g_{th} &= \frac{r}{n_a L_a} C(\lambda) \end{aligned} \quad (3.28)$$

Eq. 3.28 leads to the definition of two main quantities:

- the imaginary part, once is set equal to 0 leads to the definition of the allowed emission wavelengths  $\lambda_i$  of the modes:

$$-2k\Delta n_a(\lambda) = \Im \left( \frac{rC(\lambda)}{n_a L_a} \right) = 0 \implies \{\lambda_i\}; \quad (3.29)$$

- the real part, leads to the corresponding power threshold gain:

$$g_{th}(\lambda) = \Re \left( \frac{rC(\lambda)}{n_a L_a} \right). \quad (3.30)$$

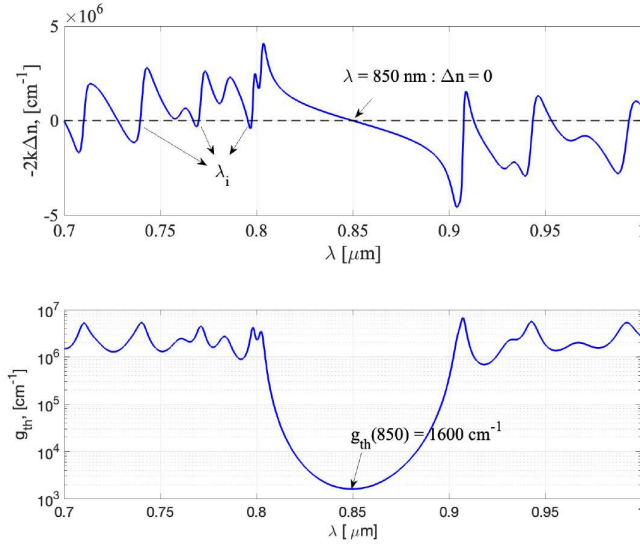


**Figure 3.6:** Dispersion curves for the VCSEL structure.

## 3.2 Vectorial VELMS 1D: generalization of the transmission matrix of a layer

This work focus on the analysis of optical anisotropies introduced into the standard VCSEL structure, that must be modelled also from the mathematical point of view. For this purpose, a generalization of the previous description must be provided, the so-called Vectorial VELMS model. Involving into the description the presence of optical anisotropies means that each layer can be characterised by two different refractive index along two different orthogonal directions.

Referring to the standard VCSEL structure described in the previous section, it must be modified adding the presence of anisotropies, namely the elasto-optic and electro-optic effects, [20] and the presence of sub-wavelength gratings [21], [22], [23].

### 3.2.1 Mathematical description of anisotropies

This section is devoted to the mathematical description of the dielectric permittivity of an anisotropic material layer. The permittivity tensor  $\Delta\epsilon$  describing a certain layer can be written as a mean value  $\pm$  a certain variation, where the mean value refers to the isotropic term, whereas the variation to the anisotropic case. Delving into the expression of the anisotropic contribution, if a certain layer is considered to be anisotropic along the x and y directions its permittivity can be written as a function of two terms, namely  $\epsilon_x$  and  $\epsilon_y$ .

This means that the refractive index characterizing each layer has two terms:

$$n_x = \sqrt{\epsilon_x}, \quad (3.31)$$

$$n_y = \sqrt{\epsilon_y}, \quad (3.32)$$

where  $\epsilon_x$  and  $\epsilon_y$  can be evaluated using Born-Wolf model or RCWA (described in details in the following section) when dealing with sub-wavelength gratings, or taken from the elasto- and electro-optic effect formulae.

The isotropic dielectric term is evaluated as the mean value of the x and y values, while the anisotropic dielectric permittivity is evaluated as the semi-difference of the two values, yielding to

$$\epsilon_{iso} = \frac{\epsilon_x + \epsilon_y}{2} \implies n_{iso} = \sqrt{\epsilon_{iso}} \quad (3.33)$$



$$\epsilon_{ani} = \frac{\epsilon_y - \epsilon_x}{2} \implies n_{ani} = \sqrt{\epsilon_{ani}} \quad (3.34)$$

It is possible that the anisotropies can have a different orientation with respect to the VCSELs' axis reference system; for this reason the dissociation angle  $\phi$ , must be taken into account per each layer.

### 3.2.2 4x4 eigenvalue problem

Considering all the ingredients previously described, the problem that we need to solve becomes a  $2 \times 2$  eigenvalue problem where the complex eigenvalues determine both the  $g_{th}$  and the  $\lambda_i$  of the cavity; the two bi-dimensional complex eigenvectors allow the reconstruction of the field, one for each polarization mode.

To thoroughly explore the concepts of calculus, we shall first examine the fundamental principles underlying the following assertions. The new transmission matrix is a  $4 \times 4$  matrix, indicating that with  $x$  and  $y$  as the polarization coordinates, and  $F$  and  $B$  representing the forward and backward propagation directions, the matrix elements are those depicted in Figure 3.7.

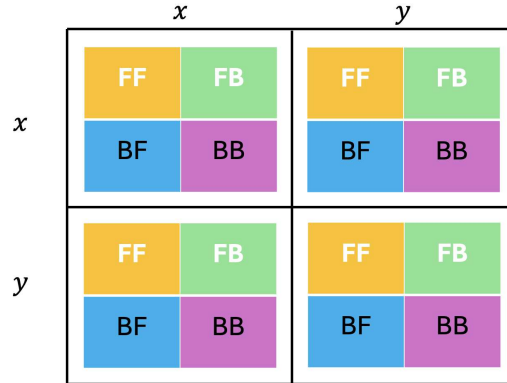


**Figure 3.7:** Generalization of  $4 \times 4$  matrix with its components.

Recalling Figure 3.4, in the previous case the only components of the field taken into account were the forward and backward, now also their behaviour with respect to the polarization must be involved. This means that for each matrix involved into the mathematical description, the FF, FB, BF, BB components are four. In particular, for the FF case the elements in position (1,1), (1,3), (3,1) and (3,3) must be considered.

We are now finally ready to solve the problem. Recalling eq. 3.3 and knowing that, in general,  $\underline{\underline{T}} = \exp(\underline{\underline{M}}L)$  it is important to re-define expression of  $\underline{\underline{M}}$  when anisotropies are considered; in particular

$$\underline{\underline{M}} = \underline{\underline{M}}_{iso} + \underline{\underline{M}}_{ani} + \underline{\underline{D}}. \quad (3.35)$$

Let's analyse each contribute one per time:

- $\underline{\underline{M}}_{iso}$  reads  $\rightarrow$

$$\underline{\underline{M}}_{iso} = k_0 \cdot \underline{\underline{K}}_{iso} \cdot \delta_{iso}, \quad (3.36)$$

where

$$\underline{\underline{K}}_{iso} = k_0 \begin{bmatrix} 1 & 1 & 0 & 0 \\ -1 & -1 & 0 & 0 \\ 0 & 0 & 1 & 1 \\ 0 & 0 & -1 & -1 \end{bmatrix}, \quad (3.37)$$

and

$$\delta_{iso} = \frac{n_i^2 - r^2}{r^2}. \quad (3.38)$$

- $\underline{\underline{D}}$ , diagonal contribute, reads as

$$\underline{\underline{D}} = 2k_0 \begin{bmatrix} 1 & 0 & 0 & 0 \\ 0 & -1 & 0 & 0 \\ 0 & 0 & 1 & 0 \\ 0 & 0 & 0 & -1 \end{bmatrix}. \quad (3.39)$$

- $\underline{\underline{M}}_{ani}$  can be computed as:

$$\underline{\underline{M}}_{ani} = k_0 \cdot \underline{\underline{K}}_{ani} \cdot \delta_{ani}, \quad (3.40)$$

where

$$\underline{\underline{K}}_{ani} = \begin{bmatrix} +\cos 2\phi & +\cos 2\phi & +\sin 2\phi & +\sin 2\phi \\ -\cos 2\phi & -\cos 2\phi & -\sin 2\phi & -\sin 2\phi \\ +\sin 2\phi & +\sin 2\phi & -\cos 2\phi & -\cos 2\phi \\ -\sin 2\phi & -\sin 2\phi & +\cos 2\phi & +\cos 2\phi \end{bmatrix}, \quad (3.41)$$

and

$$\delta_{ani} = \frac{\Delta\epsilon_{ani}}{r^2}, \quad (3.42)$$

being  $\phi$  the angle of rotation of the axes along which the refractive indexes are defined with respect of the reference system  $(x, y)$ .

The aforesaid quantities refer to a single layer, so once the  $\underline{\underline{M}}$  matrix is evaluated for the top, active and bottom regions, the solution of the problem is performed exactly with the same steps described in Section 3.2. The only difference is associated to the step of eq. 3.26, being now a real eigenvalue problem to be solved. The solution of the aforementioned problem returns a diagonal matrix with the eigenvalues and another matrix whose columns eigenvectors for the field vector.

### 3.3 Figures of merit

Once the eigenvalue problem is solved, two modes turn out as solution associated to the lasing mode and the first non-lasing higher mode. Each of these modes are characterized by an eigenvector with x and y components of the field that will be used to determine the degree of polarization, by an emitting wavelength and a threshold gain. The mode that has the lower threshold gain is the lasing one. The difference with respect to the non-vectorial case rely in the fact that now the eigenvector is non-trivial, in the sense that it has two different components; whereas in the first case the two terms were identical thus leading to a single value of wavelength and threshold gain.

Many applications require VCSELs with single mode emission; to do so it is important to ensure that the two modes are sufficiently distant. For this purpose, important parameters can be introduced:

- threshold gain difference  $\rightarrow \Delta g = \frac{g_{th_H} - g_{th_L}}{g_{th_L}} \cdot 100$ , [%] is the threshold gain splitting between lasing and non-lasing modes; where  $g_{th_H}$  is the highest value of threshold gain, whereas  $g_{th_L}$  is the lowest value. A typical value is a  $\Delta g \geq 10\%$ .
- frequency splitting  $\rightarrow \Delta f = \frac{\lambda_2 - \lambda_1}{\lambda_1 \lambda_2} c$ , [GHz], is defined as the splitting in frequency of the two modes; being  $\lambda_1$  and  $\lambda_2$  the wavelength associated respectively to the lasing and non-lasing mode and  $c$  is the speed of the light. An acceptable value of  $\Delta f$  must be of the order of tens of GHz.

## Chapter 4

# Grating optical models

The optical theory is based on the Maxwell's equations, that in the frequency domain are written as

$$\nabla \times \underline{\mathbf{E}}(\underline{r}, \omega) = -i\omega \underline{\mathbf{B}}(\underline{r}, \omega), \quad (4.1)$$

$$\nabla \times \underline{\mathbf{H}}(\underline{r}, \omega) = \underline{\mathbf{J}}(\underline{r}, \omega) - i\omega \underline{\mathbf{D}}(\underline{r}, \omega), \quad (4.2)$$

(being  $\underline{\mathbf{E}}(\underline{r}, \omega)$  and  $\underline{\mathbf{H}}(\underline{r}, \omega)$ , respectively, the electric and magnetic field phasors,  $\underline{\mathbf{B}}(\underline{r}, \omega)$  the magnetic induction phasor,  $\underline{\mathbf{D}}(\underline{r}, \omega)$  the dielectric displacement phasor and  $\underline{\mathbf{J}}(\underline{r}, \omega)$  the electric current density;  $\underline{r} = (x, y, z)$  the space vector,  $\omega$  the angular frequency and  $i$  the imaginary unit) and the constitutive equations that in the simple case of an isotropic medium are given by:

$$\underline{\mathbf{D}}(\underline{r}, \omega) = \epsilon_0 \epsilon_r \underline{\mathbf{E}}(\underline{r}, \omega) \quad (4.3)$$

$$\underline{\mathbf{B}}(\underline{r}, \omega) = \mu_0 \mu_r \underline{\mathbf{H}}(\underline{r}, \omega) \quad (4.4)$$

where  $\epsilon_0$  and  $\mu_0$  are the dielectric constant and the magnetic permeability in vacuum, whereas  $\epsilon_r$  and  $\mu_r$  the dielectric constant and the magnetic permeability typical of the material under consideration. These expressions take into account a medium that is electrically and magnetically isotropic, but in general materials are anisotropic, thus Eq. 4.3 becomes more complex. Let's focus only in the expression of the dielectric displacement  $\underline{\mathbf{D}}(\underline{r}, \omega)$  that generalizes as (for compactness let's remove the angular frequency dependence):

$$\begin{cases} D_x = \epsilon_{xx}E_x + \epsilon_{xy}E_y + \epsilon_{xz}E_z \\ D_y = \epsilon_{yx}E_x + \epsilon_{yy}E_y + \epsilon_{yz}E_z \\ D_z = \epsilon_{zx}E_x + \epsilon_{zy}E_y + \epsilon_{zz}E_z \end{cases} \quad (4.5)$$

thus the dielectric constant becomes a tensor quantity. Once anisotropies are taken into account, more complex expressions must be involved into the mathematical description of the system; complete and details are provided into [24]; however in

this chapter the important results useful for the understanding of the following explanation are provided.

It can be shown, through some considerations, that the dielectric constant tensor must be symmetric, therefore it is possible to set  $\epsilon_{ij} = \epsilon_{ji}$ , which allows to reduce the number of components from nine to six. A further reduction is possible considering a coordinate system in which the extradiagonal elements  $\epsilon_{ij}$  are zero; so that Eq. 4.5 can be written into a matrix form as:

$$\begin{bmatrix} D_x \\ D_y \\ D_z \end{bmatrix} = \begin{bmatrix} \epsilon_{xx} & 0 & 0 \\ 0 & \epsilon_{yy} & 0 \\ 0 & 0 & \epsilon_{zz} \end{bmatrix} \begin{bmatrix} E_x \\ E_y \\ E_z \end{bmatrix} \quad (4.6)$$

where  $\epsilon_{xx}$ ,  $\epsilon_{yy}$  and  $\epsilon_{zz}$  are the *principal dielectric constants* or *principal permittivities* that can be written also in a more compact way as  $\epsilon_x$ ,  $\epsilon_y$  and  $\epsilon_z$ .

The goal of this chapter is the explanation of the mathematical description of gratings. Different models related to different degrees of accuracy will be proposed in order to investigate the conditions and the operating regions for which each description model is valid.

## 4.1 Optical classification of crystals

In optics, when a beam of light passes through a certain material, a part of it can be absorbed or reflected, depending on different parameters involved, according to the Snell's law [25]. The refractive index,  $n^i$ , is the parameter that determines the amount of light that is reflected when reaches the interface of the material. It can also be seen as the factor by which the speed and the wavelength of the incoming light is attenuated with respect to the original vacuum value. Without entering too much in details on this, the properties for which the refractive index vary according to the wavelength is at the basis of the dispersion phenomenon, whose core concept is widely exploited in electromagnetic fields. According to the kind of material on which the incoming beam passes, different properties can be exploited: if a certain material transmit a single beam, according to the Snell law it is said to be *monorifrangent*; otherwise if the incoming beam after passing through the beam is splitted into two, is said to be **birefringent**.

Let's focus the attention on birefringent crystals, once the incoming beam penetrate into the material it is splitted into two components: one orthogonal to the surface, known as *ordinary component*, and the other that is the *extraordinary component*; a sketch is represented in figure 4.1.

When anisotropies are taken into account, birefringent crystals can be classified into three distinct groups based on their optical properties:

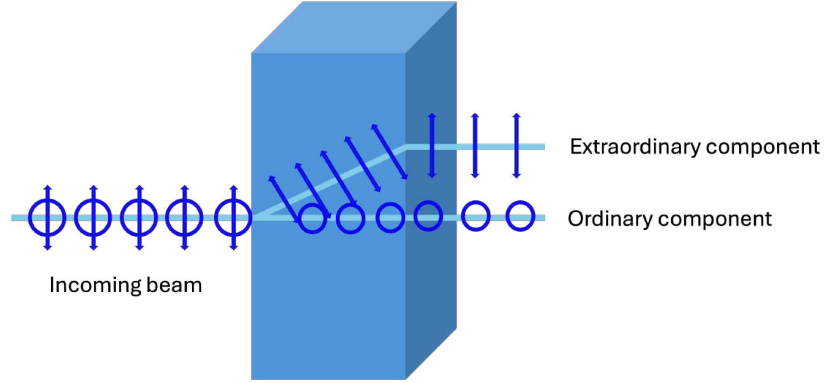


**Figure 4.1:** Birefringence mechanism of crystals.

- Group I: This includes crystals in which three crystallographically equivalent, mutually orthogonal directions can be chosen. Here the equivalent directions coincide with the principal dielectric axes  $\epsilon_x = \epsilon_y = \epsilon_z$ , resulting in  $\overline{D} = \epsilon \overline{E}$ , making the crystal optically isotropic and behaving like an amorphous body.
- Group II: This group consists of crystals where two or more crystallographically equivalent directions can be identified in one plane, namely for instance  $\epsilon_x = \epsilon_y \neq \epsilon_z$ ; so that the crystal is said to be optically uniaxial. Examples of common crystals of this kind are the trigonal, tetragonal, and hexagonal systems.
- Group III: This includes crystals where no crystallographically equivalent directions can be chosen, namely  $\epsilon_x \neq \epsilon_y \neq \epsilon_z$ . These are the crystals belonging to the orthorhombic, monoclinic, and triclinic systems. In these crystals, the directions of the dielectric axes may not be determined by symmetry and may be wavelength-dependent; crystals in this group are said to be optically biaxial.

All crystals can be classified into one of these three groups based on their optical properties. The important aspect to emphasize from the previous analysis is that the refractive index that characterised each material is subjected not only by the value of the wavelength of the incoming beam, but also by the polarization and direction of propagation of the light.

## 4.2 Born and Wolf model

Crystal's birefringent characteristics can be explained in terms of anisotropic electrical properties that leads to the definition of two different values of refractive

indexes. Nevertheless, birefringence may arise from anisotropy on a scale much larger than molecular when there is an ordered arrangement of similar particles or optically isotropic material whose size is larger compared with the dimensions of molecules, but small compared with the wavelength of light [24]. Thus this model will be employed in this work for the description of sub-wavelength gratings (see Section 4.3), where the grating can be treat as an anisotropic medium.

Let's analyse a simple case with regular stack of thin parallel plates, characterized by a fill dielectric constant  $\epsilon_1$ , alternated spacers characterized by dielectric constant  $\epsilon_2$ . The thickness  $t_1$  and  $t_2$  associated to the two regions are the ones depicted in Figure 4.2.

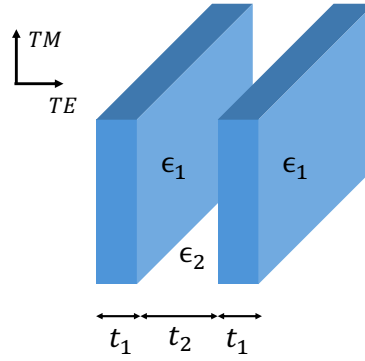


**Figure 4.2:** Relevant quantities for the model deascription.

Suppose that a plane wave hits the plates such that  $\underline{E}$  is perpendicular to the plates. Let's introduce an important simplification: the linear dimensions of the faces of the plates are assumed to be large, but  $t_1$  and  $t_2$  are small with respect to the incoming wavelength, so that  $\underline{E}$  within the spacers is considered to be uniform.

It is essential to guarantee that the normal component of the dielectric displacement must be continuous across two differential medium with the same value  $D$ . Therefore,  $\underline{E}_1$  and  $\underline{E}_2$ , identified as respectively the normal electric field components in the plates and in the spacers, are:

$$E_1 = \frac{D}{\epsilon_1}, \quad E_2 = \frac{D}{\epsilon_2}; \quad (4.7)$$

whereas the mean averaged field is:

$$E_{tot} = \frac{t_1 \frac{D}{\epsilon_1} + t_2 \frac{D}{\epsilon_2}}{t_1 + t_2}. \quad (4.8)$$

The resulting effective dielectric constant  $\epsilon_{TM}$  can be written as:

$$\epsilon_{TM} = \frac{D}{E_{tot}} = \frac{(t_1 + t_2)\epsilon_1\epsilon_2}{t_1\epsilon_2 + t_2\epsilon_1}. \quad (4.9)$$

Introducing the expression of  $\eta$

$$\eta = \frac{t_1}{(t_1 + t_2)}, \quad (4.10)$$

the Eq. 4.9 can be rewritten in a more compact expression as:

$$\epsilon_{TM} = \frac{\epsilon_1\epsilon_2}{\eta\epsilon_2 + (1 - \eta)\epsilon_1} = \frac{\epsilon_1}{\eta} + \frac{\epsilon_2}{(1 - \eta)} \implies n_{TM} = \epsilon_{TM}^2. \quad (4.11)$$

In addition, considering that the incident field has its electric vector parallel to the plates, the tangential component of  $\underline{E}$  must be continuous across the surfaces' discontinuities; this means that the value of the electric field inside the plates and in the spacer must be equal, i.e.  $E$ . Thus the parallel component of the electric displacement in the two regions are:

$$D_1 = \epsilon_1 E, \quad D_2 = \epsilon_2 E. \quad (4.12)$$

Hence the mean dielectric displacement is:

$$D_{mean} = \frac{t_1\epsilon_1 E + t_2\epsilon_2 E}{t_1 + t_2}. \quad (4.13)$$

Consequently, the effective dielectric constant is given by:

$$\epsilon_{TE} = \frac{D_{mean}}{E} = \frac{t_1\epsilon_1 + t_2\epsilon_2}{t_1 + t_2} = \eta\epsilon_1 + (1 - \eta)\epsilon_2 \implies n_{TE} = \epsilon_{TE}^2. \quad (4.14)$$

Overall, since the effective dielectric constant is the same for all the directions parallel to the plates, but different for any normal direction to the plates, the system behaves as a uniaxial crystal.

Eq. 4.11 and Eq. 4.14 are known as Born and Wolf's equation, [24]; Figure 4.3 shows the plot of the two different refractive indexes once  $\eta$  changes within the interval  $[0,1]$ ; the result highlights the fact that the two extremities the two values of  $n_{TE}$  and  $n_{TM}$  are coincident becoming a unique value, while for different values of  $\eta$  they split in two terms, where the  $n_{TM}$  assumes always lower values than  $n_{TE}$ .

### 4.3 Grating definition

One of the main challenges of VCSELs applications was devoted, starting from 1988 [26], to the achievement of a stable polarization of the output beam. VCSELs due



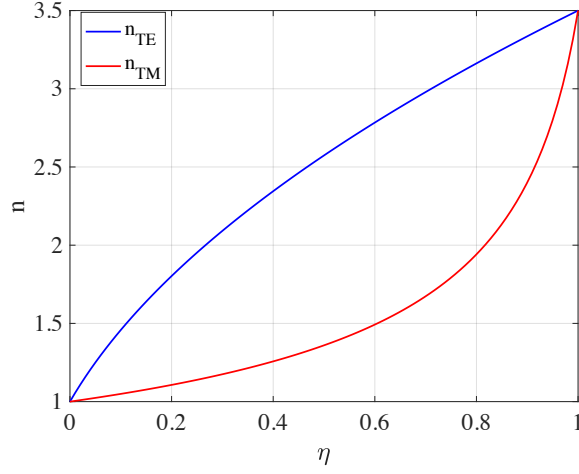


**Figure 4.3:** Born-Wolf refractive index plot in function of duty-cycle.

to their cylindrical geometry and with the presence of DBRs with a polarization independent reflectivity, do not guarantee a perfect selection in terms of polarization. Nevertheless, polarization-stable VCSELs are needed for many applications, in different domains, thus laying the basis for the continuous researches in this field.

There have been developed different strategies to obtain a stable polarization, discussed in [21], but in this work the attention has been focused on the integration on the outcoupling aperture with monolithically integrated linear grating, that have been proposed for the first time in [22] and [23], where the effectiveness of using gratings in providing a stable and predictable polarization of the emitted light has been demonstrated.

Among the different kind of gratings available, the ones suited for these applications are the **sub-wavelength gratings (SWG)** where assuming  $\Lambda$  to be the grating period, it is much smaller than the travelling wavelength. In this case, the grating behaves as an homogeneous material made of an equivalent birefringent material because it does not diffract waves and the power is evenly distributed. Within these hypothesis, the refractive indexes of the equivalent material can be approximated using the Eq. 4.11 and Eq. 4.14, described by the Born and Wolf's equations.

However, fabricating SWG and even deep SWG is not practical, in particular considering telecom wavelengths, because even with a 50% of duty cycle ( $\eta$ ) the required feature sizes of the order of tens nm are at the limit of e-beam lithography. For higher and more practical periods the aforementioned formulas provide an estimation of the equivalent indexes, but can not be considered accurate any more;

thus a rigorous description must be provided using the modal analysis.

## 4.4 Rigorous Coupled Wave Analysis - RCWA

The diffraction of electromagnetic waves by periodic structures can be computed by means of the **rigorous coupled-wave analysis (RCWA)**, a method that analyzes the grating structure and the electromagnetic field scattered by the structure itself. Once a grating with a small period is considered, higher - order waves are cut-off, so that the structure can be approximated as an homogeneous uniaxial material whose refractive indexes are obtained by solving the transcendental equations; but when the structure is more complicated, higher-order solution must be considered into the problem.

RCWA provides an exact solution of Maxwell's equations for the electromagnetic diffraction by grating structures. As a non-iterative, deterministic approach, the accuracy of the results depends solely on the number of terms used in the spatial harmonic expansion, ensuring energy conservation throughout. The solution method is based on two important criteria for the numerical stability: energy conservation and the convergence to the proper solution with an increasing number of field harmonics.

In [27] the RCWA method is analysed in details, nevertheless in this section the relevant details are going to be introduced. The system under analysis, is the one depicted in Figure 4.4 where a linear polarized electromagnetic wave with a generic incident angle of  $\theta$  and wave-vector  $k$ , hits a grating bounded between two different media with dielectric permittivities  $\epsilon_1$  (air) and  $\epsilon_2$  (generic material).

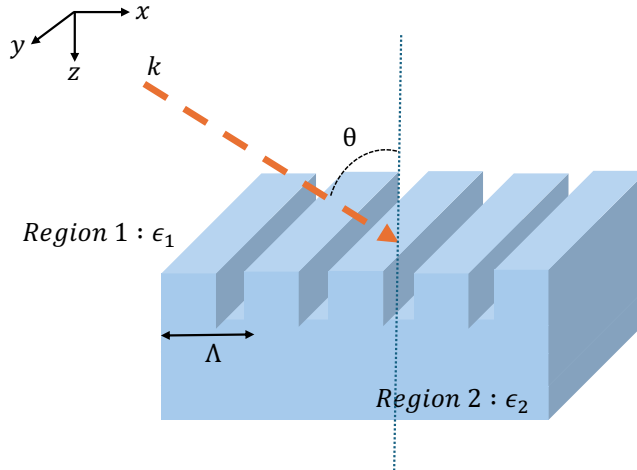


**Figure 4.4:** RCWA schematic model.

The periodic permittivity within the grating region is described in terms of a Fourier series as:

$$\epsilon(x) = \sum_h \epsilon_h \exp\left(j \frac{2\pi h x}{\Lambda}\right) \quad (4.15)$$

where the terms  $h$  are the  $h^{th}$  Fourier component of the relative permittivity in the grating region. The approach used is the solution of the Maxwell's equation in the input, grating and output regions so that the tangential electromagnetic field components are matched imposing some boundary conditions.

All the simulations results that are going to be described in the next chapters have been performed using this method that is the most accurate. In particular, the expression of the transmission matrix of each single layer composing the VCSEL structure is required (see Eq. 3.3) thus also the one that refers to the grating. The last can be evaluated by means of RCWA once the simplification of the treatment of the grating as an anisotropic layer is not valid any more.

## 4.5 Homogenization model

The theory discussed in the previous Section 4.2 is valid only when  $\Lambda \ll \frac{\lambda}{n}$ , so that changes in the refractive index differences between the grating and the empty layer are appreciable only when the duty cycle  $\eta$  changes, not the period. Moreover, the effects of changes in the grating's period can be estimated using RCWA, which affects some modal characteristics such as threshold gain, Stokes parameters, or the transmission matrix. Even though the RCWA method is highly accurate, it is not straightforward to quickly understand the effects of changes in the grating period on the refractive index values.

For these reasons, an intermediate approach has been developed: **homogenization**. The core concept of this model begins with the transmission matrix of a certain grating layer (previously obtained using RCWA), which represents a specific homogeneous and anisotropic equivalent layer described by the aforementioned transmission matrix. Since, as demonstrated in Section 4.2, a homogeneous and anisotropic layer can be described in terms of effective indices, all the treatments performed in the original case can now be reproduced, but incorporating all the properties that define the grating, including the period  $\Lambda$ . In fact, the following results will demonstrate this statement, emphasizing that the grating period is the crucial parameter that affects the validity of this model. Only sub-wavelength gratings will fully comply with this model. As  $\Lambda$  is progressively increased, the model loses its validity, as it will no longer be possible to reproduce the input transmission matrix using a homogeneous and anisotropic layer, thus requiring

RCWA for analysis.

Let us investigate the significance of this, in order to highlight the dependence of the refractive index in terms of grating's period. Recalling the CMT formalism used in order to write the transmission matrix of a homogeneous and anisotropic layer deeply described in Section 3.2.3, the coupling matrix for a vectorial 4x4 problem reads as:

$$\underline{\underline{M}} = \underline{\underline{M}}_{iso} + \underline{\underline{M}}_{ani} + \underline{\underline{D}} \quad (4.16)$$

and the transmission matrix is, where  $L$  is the grating's length:

$$\underline{\underline{T}} = \exp(\underline{\underline{M}}L) \quad (4.17)$$

Once the transmission matrix is computed it is possible to obtain the anisotropic layer's parameters that turns out exactly that transmission matrix. To do so, and obtaining as result the values of  $\epsilon_x$  and  $\epsilon_y$  it is necessary to transform the grating into a homogeneous and anisotropic layer, thus performing the homogenization. Starting from Eq. 4.17 by inverting the expression, it is possible to extract the 4x4 coupling matrix as:

$$\underline{\underline{M}} = \frac{1}{L} \log(\underline{\underline{T}}) \quad (4.18)$$

This step is mathematically correct since having a generic matrix  $\underline{\underline{A}}$  and being it diagonalizable so that:

$$\underline{\underline{A}} = \underline{\underline{V}}^{-1} \underline{\underline{D}} \underline{\underline{V}} \quad (4.19)$$

where  $\underline{\underline{V}}$  is the eigenvectors matrix and  $\underline{\underline{D}}$  is the diagonal matrix of eigenvalues  $\lambda_i$ ; then a generic transcendental function of  $\underline{\underline{A}}$  can be written as:

$$f(\underline{\underline{A}}) = \underline{\underline{V}}^{-1} \begin{bmatrix} f(\lambda_1) & 0 & 0 & 0 \\ 0 & f(\lambda_2) & 0 & 0 \\ \dots & \dots & \dots & \dots \\ 0 & 0 & 0 & f(\lambda_i) \end{bmatrix} \underline{\underline{V}} \quad (4.20)$$

Recalling once again the complete expression of  $M$  in Eq. 4.16 it is possible to explicitly write the terms  $M_{1,1}$  and  $M_{3,3}$  as:

$$M_{1,1} = \delta_{iso} k_0 + \delta_{ani} \cos(2\phi) k_0 + 2k_0 \quad (4.21)$$

$$M_{3,3} = \delta_{iso} k_0 - \delta_{ani} \cos(2\phi) k_0 + 2k_0 \quad (4.22)$$

This leads to a 2x2 system, whose unknowns are  $\delta_{iso}$  and  $\delta_{ani}$ ; it is also possible, for simplicity, to fix  $\phi$  the angle at which the anisotropy is rotated to a null value; however, in general, the system reads:

$$\begin{bmatrix} 1 & \cos(2\phi) \\ 1 & -\cos(2\phi) \end{bmatrix} \begin{bmatrix} \delta_{iso} \\ \delta_{ani} \end{bmatrix} = \begin{bmatrix} \frac{M_{1,1}}{k_0} - 2 \\ \frac{M_{3,3}}{k_0} - 2 \end{bmatrix} \quad (4.23)$$

Solving the previous system it is possible to find the values of  $\delta_{iso}$  and  $\delta_{ani}$  that turns out the original transmission matrix. Few steps are required in order to totally solve the problem, thus let's write the explicitly form of the two quantities under investigation and make some easy steps:

$$\delta_{iso} = \frac{\epsilon_{iso} - r^2}{r^2} \implies \epsilon_{iso} = \delta_{iso} r^2 + r^2 = r^2(\delta_{iso} + 1) \implies \frac{\epsilon_{TE} + \epsilon_{TM}}{2} = r^2(\delta_{iso} + 1) \quad (4.24)$$

$$\delta_{ani} = \frac{\Delta\epsilon}{r^2} \implies \Delta\epsilon = r^2\delta_{ani} \implies \frac{\epsilon_{TE} - \epsilon_{TM}}{2} = r^2\delta_{ani} \quad (4.25)$$

Once again, a 2x2 system has been obtained:

$$\begin{bmatrix} 1 & 1 \\ 1 & -1 \end{bmatrix} \begin{bmatrix} \epsilon_{TM} \\ \epsilon_{TE} \end{bmatrix} = 2r^2 \begin{bmatrix} \delta_{iso} + 1 \\ \delta_{ani} \end{bmatrix} \quad (4.26)$$

by solving it the dielectric permittivities can be achieved and finally, performing a root square the values of the refractive indexes can be evaluated.

## 4.6 Limits of the homogenization model

The theory discussed in the previous section, is correct but has some validity ranges of operation. Let's consider, for example, the structure depicted in Figure 4.5 where the value of the duty cycle  $\eta$  is fixed to 0.5, and the analysis have been performed for different values of  $\Lambda \in [0, 300] * 10^{-3} \mu m$ .

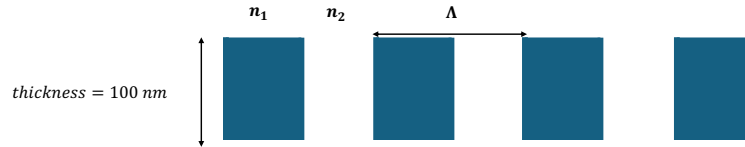


**Figure 4.5:** Grating structure under analysis

In Figure 4.6 the results of the analysis on the values of the refractive indexes, performed firstly using the Born and Wolf model (i.e. using the equations discussed in Section 4.2) and secondly according to the homogenization model, are plotted in order to perform a comparison between the two.

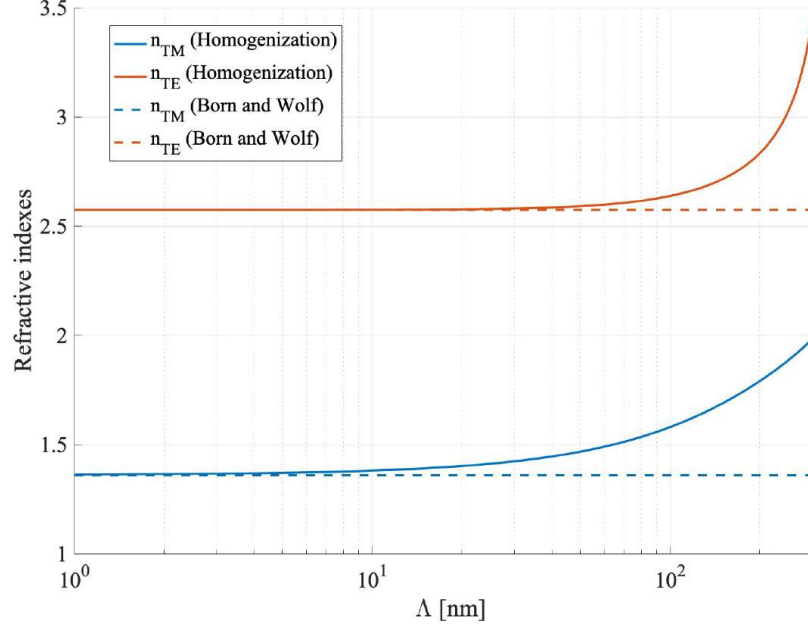


**Figure 4.6:** Homogenization and Born and Wolf models comparison

Once the grating period changes, the values of the refractive indices described in terms of the Born and Wolf model remain constant, since, once again, it is important to emphasize that according to that model the values are independent of  $\Lambda$ . Moreover, the two models yield the same results when the grating period is small; however, as it is progressively increased, the results from the homogenization model start to diverge, becoming more accurate and showing a clear dependence on  $\Lambda$ .

Even though the homogenization model appears to work well, it has some limitations. When the grating's thickness exceeds certain limits (around 120-130 nm) and at the same time the period increases (around  $10^2 - 10^3$  nm), the model is no longer valid, as the grating layer can no longer be approximated as an effective anisotropic and uniform layer (recall that this is a key hypothesis for the model's validity), regardless of the parameters used. This also means that it cannot be described in terms of a 1D model, as higher-order waves are not taken into account. Therefore, a more precise analysis, namely RCWA, must be performed to derive the transmission matrix expression.

## Chapter 5

# Design strategies for circular polarization emission

The idea of having stable output polarized light for VCSELs is a crucial aspect that has been discussed for years in order to achieve good results in the previously mentioned applications, where stable CP is required. The first and most common approach used to obtain a CP-VCSEL involves a linearly polarized VCSEL combined with a quarter-wave plate, resulting in a bulky and costly setup that requires careful assembly for proper operation, which is not particularly suitable or easy to manage. Starting from this, many attempts have been proposed to reduce the volume of these devices as much as possible, using different approaches, in particular:

- 3D laser displays play an important role in next-generation display technologies due to the ultimate visual experience they provide. CP lasers are attractive for these purposes as they enhance the contrast ratio and comfort. 3D laser displays with CP have been discussed in [28], where **cholesteric liquid crystal (CLC)** arrays have been employed. CLCs are a particular type of crystal characterized by a helical structure, where molecules progressively change their orientation along the helix. This interesting structure exhibits the capability to selectively reflect light with a certain wavelength (equal to the helix pitch) into circular polarization. This property, known as selective reflection, leads to interesting optical properties useful for displays, such as the ability to emit high-contrast colored light. However, this technology has only been experimented with in the last three years, so not many experimental data are available for a complete analysis, especially for its employment in other applications.
- In [29] another attempt has been proposed by integrating a standard VCSEL with a **solid-state chiral sculptured thin film (CSTF)** to control the

polarization of the laser output, as shown in Figure ???. Specifically, the top DBR is superimposed by a columnar thin film that works as a quarter-wave plate, and by a CSTF that acts as a chiral mirror on top (working with a chiral mirror means that an object can be superimposed onto its mirror image). The CSTF consists of a stack of identical and parallel nano-helices. The interaction between the linear birefringence and the chirality of the CSTF structure results in a particular effect: when the CSTF is excited with a light beam whose wave vector is aligned parallel to the nano-helix, CP light with the same chirality as the CSTF is reflected, while light with opposite chirality is reflected back. Although this structure shows interesting results, it is very complex from a technological point of view, adding additional components and fabrication steps that are not easy to control.

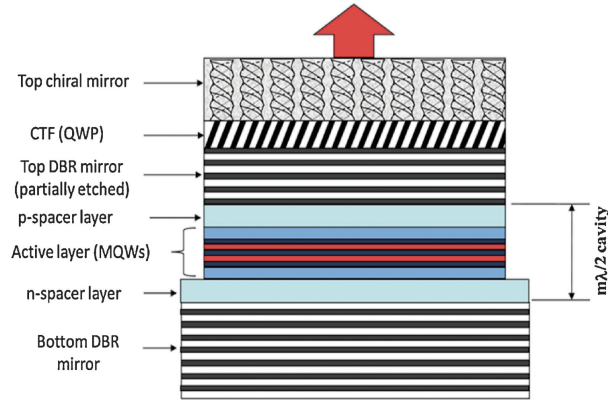


**Figure 5.1:** Schematic of a VCSEL with CTF and a CSTF [29].

- In the context of exploiting dielectric meta-surfaces, which are attractive due to being ultra-thin, having low absorption loss, and being easy to manipulate, including for polarization control, a meta-surface integrated VCSEL structure was presented in [30]. The innovation of the aforementioned structure lies in the replacement of the VCSEL's top reflector with a **chiral high-contrast meta-surface** to control the output light polarization (see Figure ??). This particular structure consists of gammadion-shaped GaAs nanostructures arranged in a square lattice on top of an aluminum oxide spacer. Using this structure, a degree of nearly 60% circular polarization was achieved, making it one of the most promising technologies even for commercial applications.
- In [31] another approach has been investigated considering the chirality of the entire resonator, in such a way an anisotropic layer that considered sole is achiral, when its axes are tilted make the entire cavity chiral. The structure



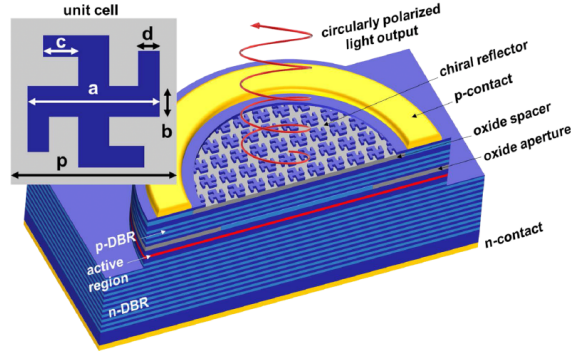


**Figure 5.2:** VCSEL schematic featuring a chiral meta-surface as the top reflector. The top-left inset shows a top view of the meta-surface unit cell, with the geometric parameters labeled [30].

under analysis, reported in Figure 5.3, is a standard VCSEL integrated with two SWGs placed at the two DBRs extremities. In this view, by manipulating the tilting angle and the grating thickness it is possible to measure the degree of circular polarization achievable even reaching arrangements for which the output beam is completely CP.

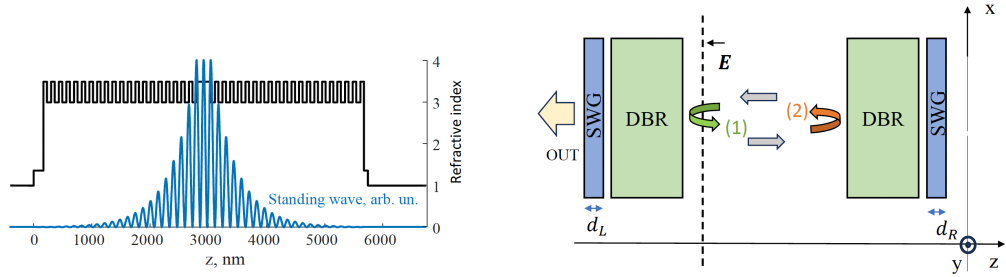


**Figure 5.3:** The left image shows the refractive index and standing wave profile of VCSEL structure; whereas the right image represents the schematics of the cavity [31].

This work's aim is to provide another possible solution for CP - VCSELs with a structure that is composed of a double-integrated gratings of different materials placed at the same side, in correspondence of the outcoupling facet, leading the basis of possible future developments on this field, even for a promising commercial production of these devices.

## 5.1 Poincarè sphere and Stokes parameters

Before exploring the description of this new structure (provided in Section 6.2) it is important to define by the mathematical point of view what are the parameters that must be considered to ensure the realization of a CP-beam.

Let's consider a monochromatic light beam that propagates within an isotropic and homogeneous medium described by means of:

$$\overline{E} = \overline{E}_0 \cos(\omega t - \vec{k}\vec{r}), \quad (5.1)$$

where  $\overline{E}_0$  is the amplitude vector,  $\omega$  is the angular frequency and  $k$  is the wave-vector. Considering the time evolution of the light propagation along the  $z$  axis, the electric field vector lying in the  $xy$  plane is described as:

$$E_x(t) = E_{0x}(t) \cos[\omega t + \delta_x(t)] \quad (5.2)$$

$$E_y(t) = E_{0y}(t) \cos[\omega t + \delta_y(t)] \quad (5.3)$$

where  $\delta_x(t)$  and  $\delta_y(t)$  are the instantaneous phase terms. Delving with monochromatic waves with constant phase and amplitudes, and removing  $\omega t$  from Eq. 5.2 and 5.3, it is possible to get the expression of the polarization ellipse:

$$\frac{E_x^2(t)}{E_{0x}^2} + \frac{E_y^2(t)}{E_{0y}^2} - \frac{2E_x(t)E_y(t)}{E_{0x}E_{0y}} \cos\delta = \sin^2\delta, \quad (5.4)$$

being  $\delta = \delta_x - \delta_y$ . In order to have observables, it is possible to deal with average over time:

$$\frac{E_x^2(t)}{E_{0x}^2} + \frac{E_y^2(t)}{E_{0y}^2} - \frac{2E_x(t)E_y(t)}{E_{0x}E_{0y}} \cos\delta = \sin^2\delta. \quad (5.5)$$

Multiplying the last equation by  $4E_{0x}^2 E_{0y}^2$  it leads to:

$$4E_{0y}^2 E_x^2(t) + 4E_{0x}^2 E_y^2(t) - 8E_x(t)E_y(t) \cos\delta = (2E_{0x}E_{0y} \sin\delta)^2. \quad (5.6)$$

Recalling that

$$\langle E_x(t)E_y(t) \rangle = \lim_{T \rightarrow \infty} \frac{1}{T} \int_0^T E_x(t)E_y(t)dt, \quad (5.7)$$

terms in Eq. 5.6 become:

$$\langle E_x^2(t) \rangle = \frac{1}{2} E_{0x}^2, \quad (5.8)$$

$$\langle E_y^2(t) \rangle = \frac{1}{2} E_{0y}^2, \quad (5.9)$$

$$\langle E_x(t)E_y(t) \rangle = \frac{1}{2}E_{0x}E_{0y}\cos\delta, \quad (5.10)$$

so that Eq. 5.6 reads:

$$2E_{0x}^2E_{0y}^2 + 2E_{0x}^2E_{0y}^2 - (2E_{0x}E_{0y}\cos\delta)^2 = (2E_{0x}E_{0y}\sin\delta)^2. \quad (5.11)$$

By adding and subtracting at the left side member of the previous equation the quantity  $E_{0x}^4 + E_{0y}^4$  the final expression reads as:

$$(E_{0x}^2 + E_{0y}^2)^2 - (E_{0x}^2 - E_{0y}^2)^2 - (2E_{0x}E_{0y}\cos\delta)^2 = (2E_{0x}E_{0y}\sin\delta)^2, \quad (5.12)$$

finally, the terms in parenthesis can be written as:

$$S_0 = E_{0x}^2 + E_{0y}^2 \quad S_1 = E_{0x}^2 - E_{0y}^2 \quad S_2 = 2E_{0x}E_{0y}\cos\delta \quad S_3 = 2E_{0x}E_{0y}\sin\delta$$

so that Eq. 5.12 can be written in a more compact way as:

$$S_0^2 = S_1^2 + S_2^2 + S_3^2. \quad (5.13)$$

The previous four terms are known as the **Stokes polarization parameters**, which describe the polarization state of light. In particular,  $S_0$  describes the overall optical power without providing any relevant information about the polarization state;  $S_1 \in [-1, 1]$  and, if equal to  $\pm 1$ , describes light linearly polarized along the x or y direction, respectively;  $S_2 \in [-1, 1]$  and, if equal to  $\pm 1$ , describes light linearly polarized along  $\pm 45^\circ$ . Meanwhile,  $S_3 \in [-1, 1]$ , if equal to  $\pm 1$ , describes circularly polarized light rotating either clockwise or counterclockwise.

This means that, in order to achieve CP light, it is important to focus on the Stokes parameter  $S_3$ , ensuring it is equal to  $\pm 1$  or at least higher than  $\pm 0.95$ . This is the parameter that will be thoroughly highlighted in the next chapter.

$S_1$ ,  $S_2$ , and  $S_3$  can be plotted in 3D coordinates, forming the so-called **Poincaré sphere**, whose radius is  $P = \sqrt{S_1^2 + S_2^2 + S_3^2}$ , coinciding with  $S_0$ . The Poincaré sphere represents all possible polarization states. In Figure 5.4, relevant points are depicted: the two blue points are associated with circular polarization, the red ones refer to linear polarization at  $\pm 45^\circ$ , and the green ones define linearly polarized light both vertically and horizontally. All other points on the sphere correspond to generic elliptical polarization.

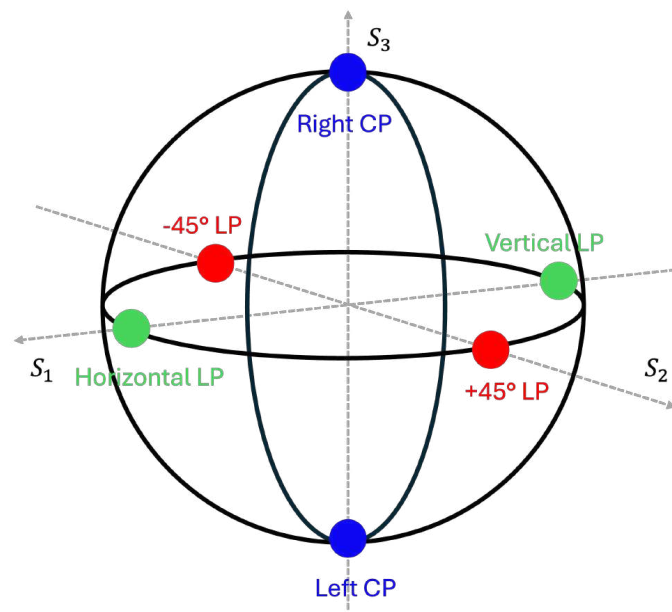


**Figure 5.4:** Poincaré sphere and relevant polarization points.

# Chapter 6

## Modeling results

### 6.1 Single grating structure

The first structure that has been analyzed, sketched in Figure 6.1, is a standard VCSEL with a grating structure placed at the outcoupling facet of the top DBR. The core concept of this analysis is to understand the important parameters related to the description of the VCSEL (emission wavelength, threshold gain, polarization) by starting from a simple structure and progressively introducing additional effects such as grating rotation, strain, and electro-optic effects, aimed at closely mimicking the correct and realistic working principles of the device.

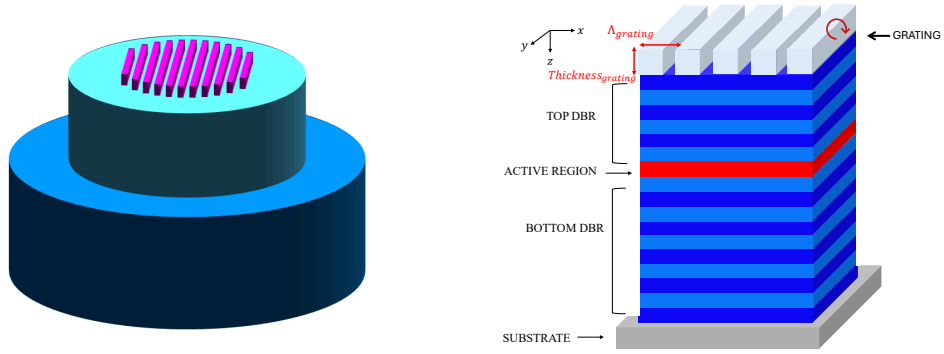


**Figure 6.1:** 3D single grating structure (left), simplified sketch with relevant parameters

#### 6.1.1 Analysis on rotated and non-rotated grating

The VCSEL structure that has been implemented in VELMS code consist of 18 and 35 pairs of mirrors for, respectively, the top and bottom DBRs. The structure

is completed introducing a grating on the outcoupling facet of the top DBR. The 1D refractive index profile of the aforesaid structure is presented in Figure 6.2.

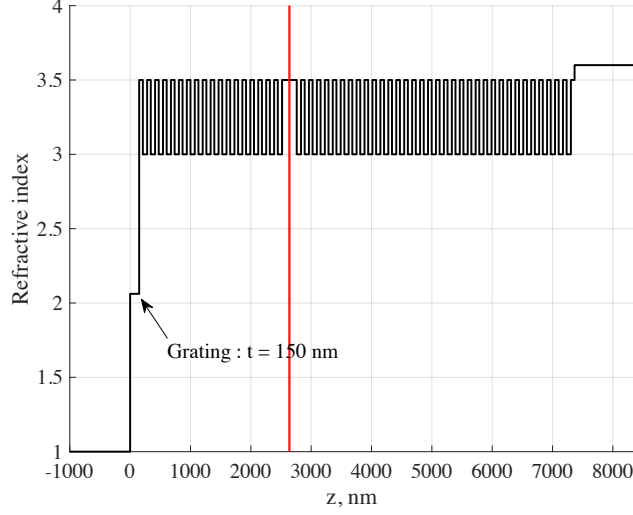


**Figure 6.2:** 1D refractive index profile of single grating VCSEL structure when  $t=150$  nm. The value of the refractive index associate is the isotropic one evaluated as  $n = \sqrt{\frac{\epsilon_{TM} + \epsilon_{TE}}{2}}$ .

In order to highlight the differences, the VELMS analysis has been performed for different values of gratings thicknesses, namely 0 nm - so no grating present at all - up to 300 nm. The resulting values of the  $\Delta f$  and  $\Delta g$  are reported in Figure 6.3. Here it is possible to see that for grating thicknesses the required conditions for  $\Delta f$  and  $\Delta g$  are not satisfied, thus thicker gratings are needed. The choice of the suitable thickness is the result of a trade-off between the two quantities. Here, thicknesses of 0, 150 and 300 nm have been considered for the analysis.

Referring to Figure 6.3 is also evident that when the grating is not present at all  $\Delta g$  is null, since the two modes have the same threshold gain, as a solution of a trivial problem as discussed in Section 3.3. The same reasoning can be performed for the value of the two emitting wavelengths, for  $t = 0$  nm, set to exactly 850.00 nm, considered as the target value so that  $\Delta f = 0$  GHz; whereas when gratings are introduced there are a small variation with respect to the target values, overall not so relevant giving rise to an appreciable value of  $\Delta f$ .

It is also interesting to observe Figure 6.4, where the evolution of the Stokes' parameters for different rotating angles and for the three grating thicknesses employed for the analysis are plotted. Specifically, in the case in which there is not the presence

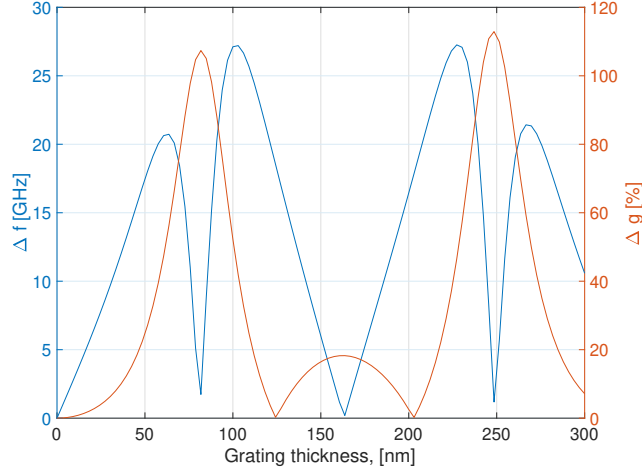


**Figure 6.3:**  $\Delta f$  and  $\Delta g$  plot for different grating thicknesses with a grating rotating angle of  $45^\circ$ .

of the grating there is a complete linear polarization of the lasing beam, since  $S_1 = +1$ . Concerning the other two cases, instead, a complete linear polarization is present when the grating is not rotated or orthogonally rotated with respect to the VCSEL's reference axes; when the grating has  $\theta = 45^\circ$  then the polarization of the lasing mode is polarized along  $-45^\circ$  and  $+45^\circ$  respectively in the case of grating thickness of 150 nm and 300 nm.

Whatever is the grating rotating angle CP is never reached highlighting once again the fact that introducing a grating into the VCSEL structure allows to obtain linear polarization either along the same direction of the VCSEL's axis structure either rotated at  $\pm 45^\circ$ . This is due to the fact that in this analysis the grating is only anisotropy introduced and since there is not the competition among different optical misaligned anisotropies the resulting polarization will always be linear.

### 6.1.2 Elasto- and electro-optic effects: theoretical explanation

When anisotropies are involved into the description of the VCSEL structure the tensor quantity  $\Delta\epsilon$ , mentioned in Chapter 4, plays an important role for their definition into the model. In this section the attention will be pointed on the anisotropy induced by the **elasto-** and the **electro-** optic effects (EOE). The validity of the introduction of these two quantities has been demonstrated in different researches [32] and [33] among the others, where the power of the manipulation

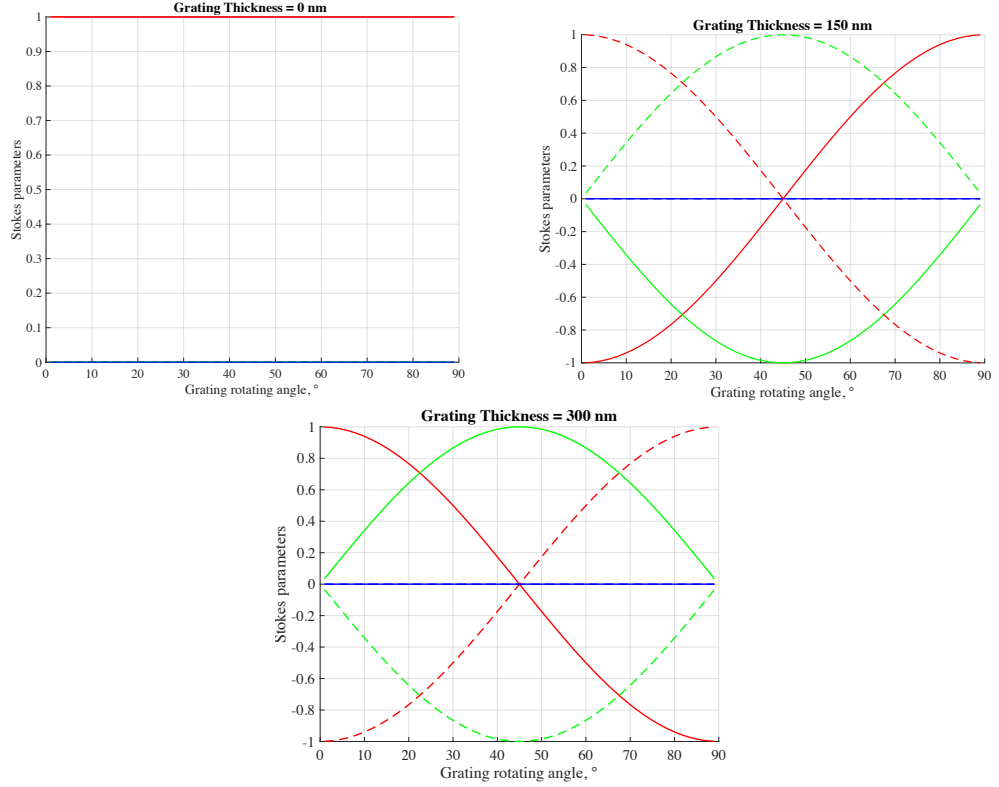


**Figure 6.4:** Stokes parameters comparison for VCSEL structures with 0, 100, 300 nm thick gratings in function of the gratings' rotating angle. In all the three plots solid lines are associated to the lasing mode, whereas the dashed lines refer to the second order mode. Red lines identify  $S_1$ , green lines  $S_2$  and the blue ones  $S_3$ .

of optical properties such as the polarization switching, the wavelength tuning as consequence of the application of anisotropic strain along specific crystallographic axes and the correspondent changing of the lattice constants of the semiconductor materials by means of the EOE have been demonstrated.

After a brief theoretical explanation of the two aforesaid anisotropies, their effects on the VCSELs structure under analysis will be demonstrated.

In order to mimic the possible presence of stress into the VCSEL structure due to technological features or intentionally applied externally, has been mimicking by means of the elasto-optic effect. The last, is induced by the strain through the relation:



$$\Delta(\eta)_i = p_{ij}\epsilon_j \quad i, j = 1, 2, \dots, 6 \quad p = \begin{bmatrix} p_{11} & p_{12} & p_{12} & 0 & 0 & 0 \\ p_{12} & p_{11} & p_{12} & 0 & 0 & 0 \\ p_{12} & p_{12} & p_{11} & 0 & 0 & 0 \\ 0 & 0 & 0 & p_{44} & 0 & 0 \\ 0 & 0 & 0 & 0 & p_{44} & 0 \\ 0 & 0 & 0 & 0 & 0 & p_{44} \end{bmatrix}, \quad (6.1)$$

where  $\Delta(\eta)_i = \Delta(\frac{1}{n_i^2})$  is the impermeability tensor,  $p_{ij}$  are the elasto-optic coefficients that relate linearly the impermeability tensor and the applied strain  $\epsilon_j$  (considering the AlGaAs crystalline structure, only the terms  $p_{44}$  are the relevant ones). It is important to notice that, the strain is considered to be uniformly distributed along the entire VCSEL structure, except in the grating layers and in the active region.

The strain is typically a stochastic quantity, whereas the EOE is a deterministic; in order to simplify the analysis, it is possible to do not introduce directly the expression of EOE and introduce an effective strain that mimic its behaviour.

Concerning the EOE, as reported in [20], it takes into account how the optical properties of a certain material, in particular, the refractive index, change in response to an applied electric field. There are two main kind of EOE, namely Pockels and Kerr. The first one, refers to a refractive index that changes linearly with respect to the amount of the electric field applied; whereas the second one refers to a quadratic relationship of the refractive index with respect to the electric field; for these purposes, the Pockels effect is the suited one. The equation that governs the EOE, written within the Einstein notation, is:

$$\Delta(\eta)_i = r_{ij}\mathcal{E}_{sj} \quad i = 1, 2, \dots, 6 \quad j = 1, 2, 3 \quad r = \begin{bmatrix} 0 & 0 & 0 \\ 0 & 0 & 0 \\ 0 & 0 & 0 \\ r_{41} & 0 & 0 \\ 0 & r_{41} & 0 \\ 0 & 0 & r_{41} \end{bmatrix}, \quad (6.2)$$

where  $r_{ij}$  are the electro-optic coefficients,  $\mathcal{E}_{sj}$  is the DC electric field along the  $j$ -direction (where 1,2,3 correspond respectively to x,y,z directions). Considering AlGaAs crystalline structure the only relevant parameter is  $r_{41}$ , thus  $r_{ij}$  simplifies as reported in the previous equation.

These two effects must be expressed in terms dielectric permittivity, the parameter that must be introduced into the mode, whose transverse diagonal expression can

be written as:

$$\Delta\epsilon_t = \begin{bmatrix} \Delta\epsilon_{xx} & 0 \\ 0 & \Delta\epsilon_{yy} \end{bmatrix} \quad (6.3)$$

The diagonal components can be written both in terms of electro-optic components or in terms of elasto-optic components as:

$$\begin{aligned} \Delta\epsilon_{xx} &= +n^4 r_{41} \mathcal{E}_{sz} \Leftrightarrow \Delta\epsilon_{xx} = -n^4 p_{44} \frac{\epsilon}{2} \\ \Delta\epsilon_{yy} &= -n^4 r_{41} \mathcal{E}_{sz} \Leftrightarrow \Delta\epsilon_{yy} = +n^4 p_{44} \frac{\epsilon}{2} \end{aligned} \quad (6.4)$$

being  $\mathcal{E}_{sz}$  the electric field along the z-direction.

For simplicity, in the following analysis, the elasto-optic anisotropy has been considered to be constant in the entire structure, with the elasto-optic coefficient set at  $p_{44} = -0.072$ , so that the dielectric permittivity associated to each layer, induced by the aforesaid phenomenon, can be written as:

$$\Delta\epsilon_{layer}^{elasto} = n_{layer}^4 p_{44} \frac{\epsilon}{2}. \quad (6.5)$$

Whereas, concerning the EOE, it is possible to write:

$$\Delta\epsilon_{layer}^{EOE} = \epsilon_{xx} - \epsilon_{yy} = 2n_{layer}^4 * r_{41} < E >_{layer} \quad (6.6)$$

being  $< E >_{layer}$ , as the mean value of the electric field evaluated by means of the drift - diffusion model normalized with respect to each layer dimension:

$$< E >_{layer} = \frac{\int_{layer} E_{DD}(z) dz}{L_{layer}}. \quad (6.7)$$

Considering both the elasto- and electro- optic effects, it is possible to write that the total dielectric permittivity refers to each layer is simply the superposition of the two :

$$\Delta\epsilon_{layer} = \Delta\epsilon_{layer}^{EOE} + \Delta\epsilon_{layer}^{elasto}. \quad (6.8)$$

### 6.1.3 Elasto-optic effects on rotated and non-rotated grating

The VCSEL structure described in Section 6.1.1, without the grating and with 150nm and 300nm thick gratings, has been analysed introducing the strain effect, into a range values of  $\epsilon \in [10^{-7}, 10^{-3}]$ . Looking at Figure 6.5 the effects of the applied strain on the device can be highlighted. Recalling that, technologically it is important that the frequency spacing between the lasing and the second order

mode should be of the order of tens of GHz ( $\sim [15, 25]$  GHz) and that at the same time, the threshold gain splitting should be higher than the 10 %, the resulting values of strain that enable to obey simultaneously to these two constraints is of the order of  $10^{-4}$ .

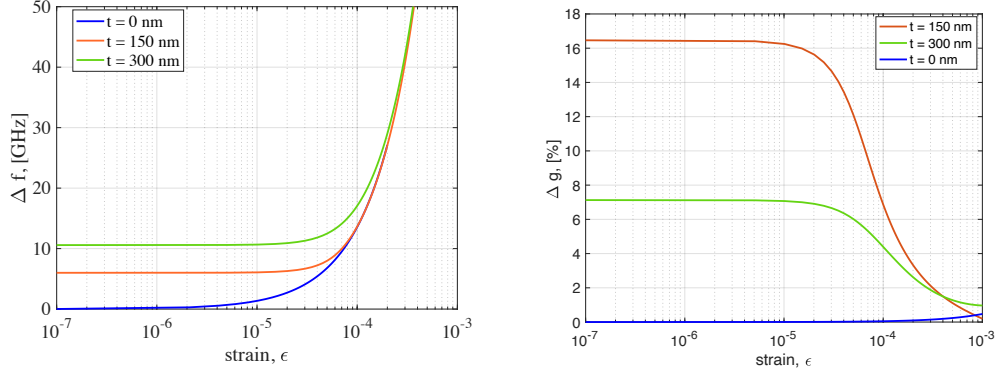
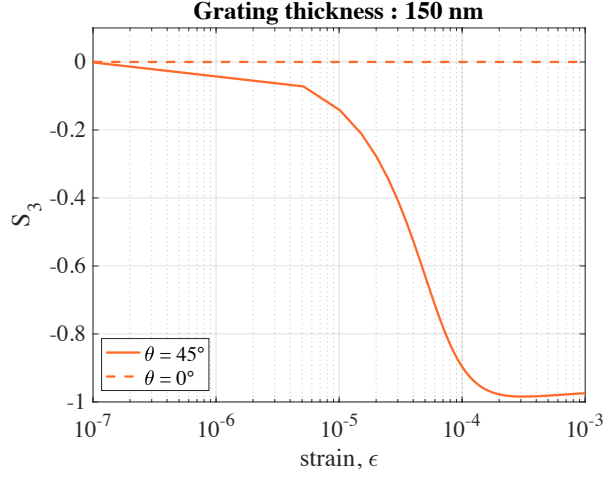


**Figure 6.5:** Frequency and threshold gain spacing comparison of VCSELs structure with 0nm, 150nm, 300nm thick gratings. In the case in which the grating is present, it has been chosen a rotating angle of  $45^\circ$ .

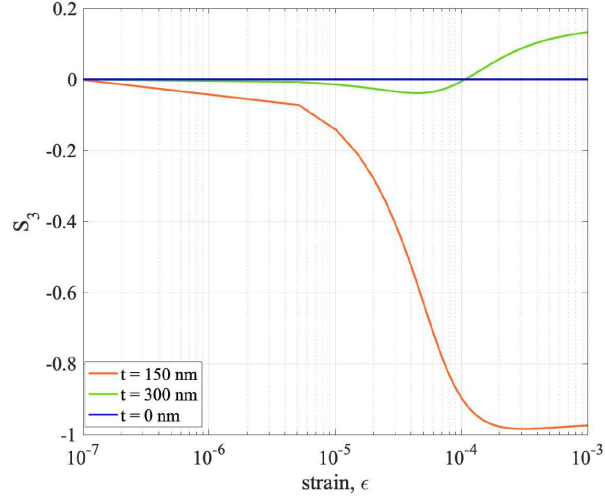
The results shown in Figure 6.4, demonstrate that by modulating the rotating angle of the grating linear polarization can be achieved for the lasing mode and that no one of the infinite combinations tested lead to CP, being  $S_3$  always null. Let's see what happens when strain is applied.

Figure 6.6 shows the evolution of the Stokes' parameter  $S_3$  with increasing value of applied strain and in two different cases with a rotating grating (150 nm thick) angle null and of  $45^\circ$ . In the first case, with a non-rotating grating, whatever is the value of the applied strain  $S_3$  remains null, thus no CP is achievable (dashed line in the plot). Whereas, in the second case, fixing the grating rotating angle and progressively increase the amount of strain the degree of CP increases up reaching a degree of - 0.97 (the sign minus stands for counter-clock wise) of CP, in this example (solid line in the plot).

The result of the previous analysis, demonstrate that CP can be obtained starting from a VCSEL with a grating whose thickness and rotating angle must be properly engineered for this purpose and subjected to a certain amount of applied strain, that once again must be of the order of  $10^{-4}$  to give the wanted results. As depicted in Figure 6.7 once the grating thickness is increased at 300nm, even applying strain the value of  $S_3$  is almost null, thus meaning that technologically particular attention must be devoted to the thickness of the grating features, being this an important drawback leading to the use of this methodology for general elliptical polarized beams.



**Figure 6.6:**  $S_3$  comparison for a VCSEL with 150nm thick grating rotated or not.



**Figure 6.7:**  $S_3$  comparison for VCSELs with different grating thicknesses.

#### 6.1.4 Electro-optic effects on rotated and non-rotated grating

In [34], we firstly demonstrate that CP-VCSELs can be obtained by introducing tilted grating with respect to crystal axes combined with electro-optic effect. The analysis have been performed investigating a standard 850 nm AlGaAs VCSEL with 20-pairs of top p-doped DBR and 35-pairs of bottom n-doped DBR. The doping levels chosen in the structure are  $3 \times 10^{18} \text{cm}^{-3}$  for the first 15 pairs of the top DBR and for the substrate and  $2 \times 10^{18} \text{cm}^{-3}$  for the remaining top and bottom

DBRs. A sub-wavelength grating, on the outcoupling faced, between GaAs and air is placed with a filling factor of 0.5 and a spatial period of 150 nm. A sketch of the refractive index profile of the aforesaid structure superimposed to the standing wave profile is depicted in Figure 6.8.

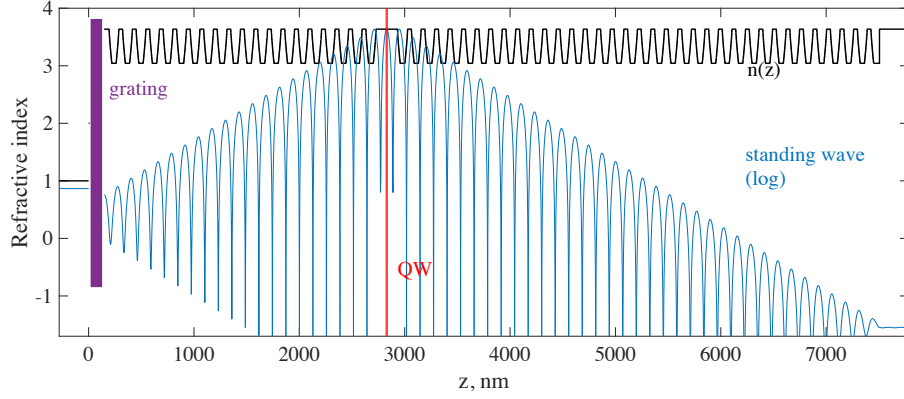


**Figure 6.8:** Refractive index profile and standing wave for a VCSEL structure with 147 nm thick grating rotated of  $53^\circ$ .

The electro-optic effect, whose equations have been discussed in Section 6.1.4, has been introduced into the model considering Pockels coefficients to 1.6pm/V and 0.78 pm/V associated respectively to GaAs and AlAs; whereas the electrostatic field profile, shown in Figure 6.9 has been obtained in terms of 1D drift-diffusion simulation [35] applying a bias of 3V. The resulting  $\Delta\epsilon_{yy}$  is shown in Figure 6.10. Involving the grating structure into the model, described in terms of RCWA, whose thickness has been chosen into the operating interval of  $t \in [0, 200]nm$  and a rotating angle of  $\theta \in [0, 90]^\circ$ , the resulting evolution of the  $S_3$  parameter is the one plotted in Figure 6.8 (right). From the vectorial analysis, the transverse modes feature different spatial distributions, in particular, in the figure regions where modulating both the grating thickness and the rotating angle CP is achievable with  $S_3 \geq 0.9$  and even more  $S_3 \geq 0.99$ , for the lasing mode. Notice that a rotation of almost  $45^\circ$  ensures a good result.

What is more, the red marker highlights the condition under which total CP is possible: employing a 147 nm grating thickness and a rotating angle of  $53^\circ$ . This condition, devoted to maximise  $S_3$  is validated also in terms of  $\Delta g = 18\%$ , whose plot is reported in Figure 6.11 (right). Dashed with lines in the figure highlight the presence of modal jumps, where  $\Delta g = 0$ .

In order to better appreciate this result, it is possible to consider the complex emission unit vector of the lasing optical field  $\hat{E} = E_x\hat{x} + E_y\hat{y}$  for a certain combination of thicknesses and rotating angle that impinge onto a linear polarizer

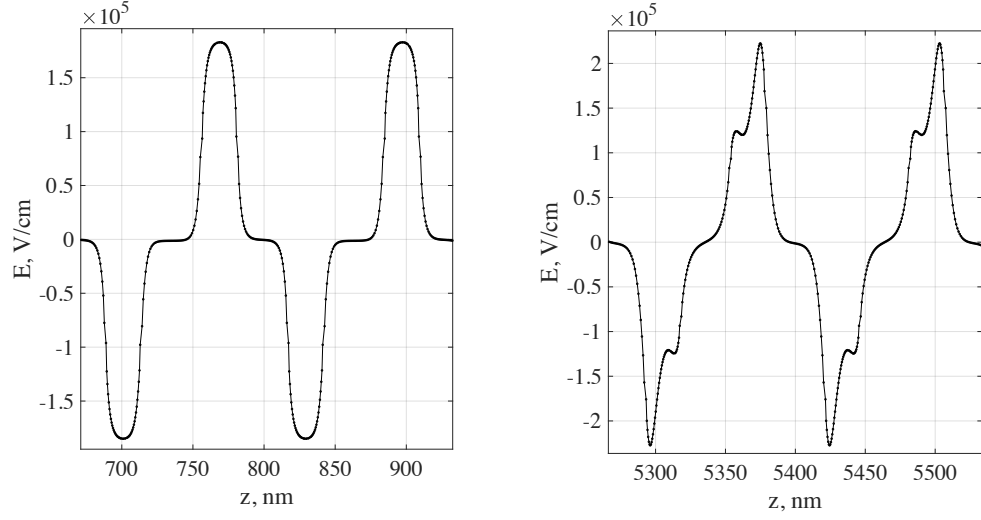


**Figure 6.9:** Electric field profile associated respectively to the top DBR (left plot) and the bottom one (right plot).

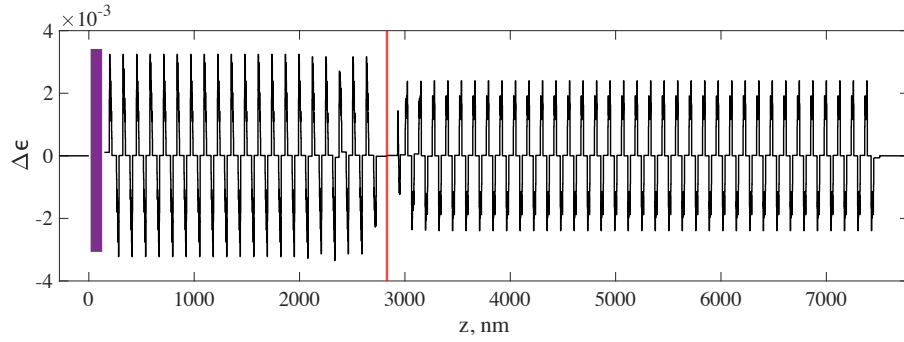


**Figure 6.10:** Dielectric constant profile into the VCSEL structure by means of electro-optic anisotropy.

whose axis is rotated with respect to  $\hat{x}$  of a certain angle  $\gamma$ . If the beam is CP the linear polarizer output must satisfy the following requirement:

$$I_{out}(\gamma) = |\hat{E} \cdot (\hat{x}\cos\gamma + \hat{y}\sin\gamma)|^2 = 0.5\forall\gamma \quad (6.9)$$

the corresponding output is reported in Figure 6.12, where the angular axis represents the polarization angle  $\gamma$ , whereas the distance from the center to the plotted curve is the output intensity of the polarizer.

The previous results have been further investigated in terms of different values of applied voltage, with  $V \in [2.5, 3.5]$  V by means of the 1D drift-diffusion analysis in order to highlight the fact that there is no a strong dependence of the results on the

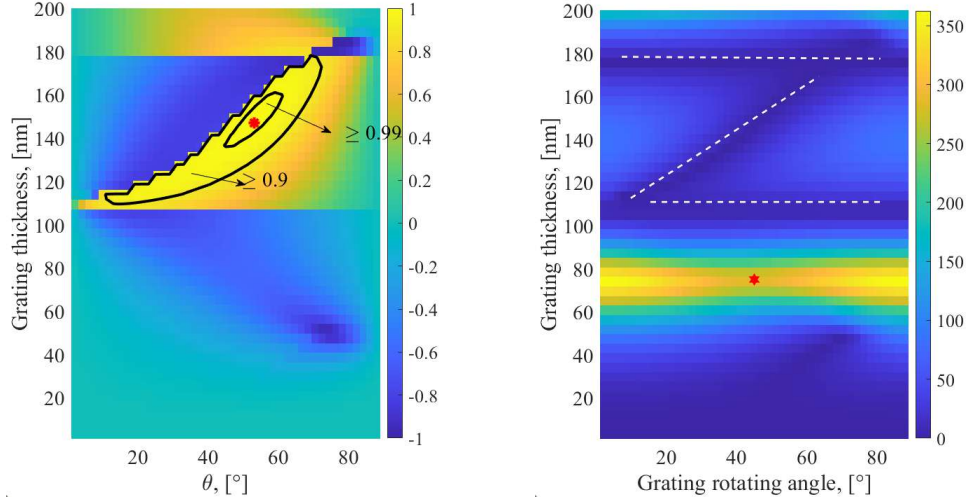


**Figure 6.11:**  $S_3$  (right) and  $\Delta g$  (left) maps, associated to the lasing mode, for different grating thickness and rotating angles. The dashed lines of the second figure emphasize modal jumps where  $\Delta g = 0$ .

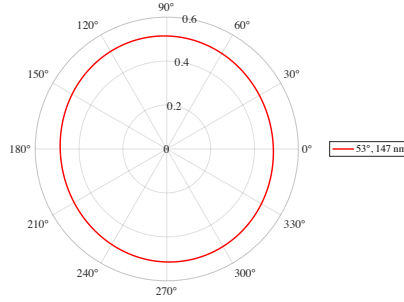


**Figure 6.12:** Linear polarizer output associated to the red marker point.

applied voltage, since the relevant quantities of interest remains almost constant. In particular, Figure 6.13 shows the evolution of  $S_3$  for bot the lasing (blue) and non lasing (red) modes in function of the value of the applied bias.  $S_3 = 1$  is appreciable whatever is the value of the applied bias (chosen into a reasonable operating range of values), highlighting that CP is not dependent on this parameter. This analysis emphasize also the fact that the electric field present into the DBRs, the one responsible of the EOE, is totally independent from the value of the applied bias.

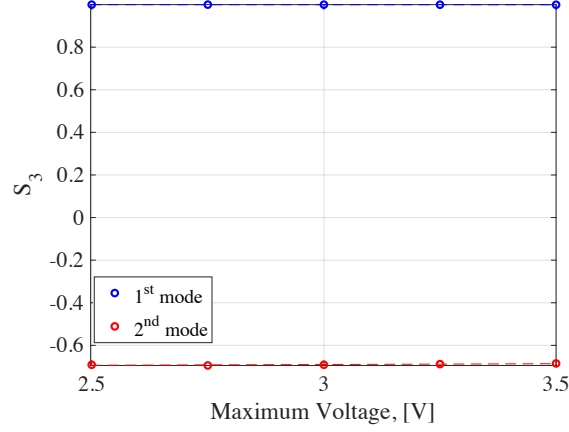


**Figure 6.13:** Analysis on different applied bias, demonstrating that CP not depends on it. Blue lines refer to lasing mode, red ones to the superior mode.

## 6.2 Double grating structure

Due to the fact that lot of times the elasto- and electro- optic effect are difficult to estimate, an implementation sufficiently independent from these intrinsic anisotropies is required. Aiming to do so, a complex design has been proposed in this thesis work. Specifically, a double grating structure with a spacer in the middle is now under analysis. Technologically, this structure can be obtained exploiting nano-imprinting lithography (NIL), an high-resolution and cost-effective technique devoted to the fabrication of nanoscale patterns, including gratings, [36]. The process involves mechanically transferring a nanoscale pattern from a mold (or stamp) onto a substrate using a pressing technique.

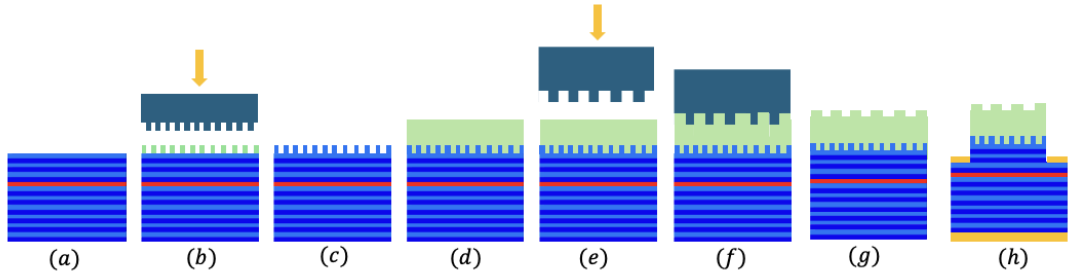


**Figure 6.14:** Double gratings VCSEL structure technological process steps.

In Figure 6.14 the main process steps devoted to the fabrication of the wanted



new structure are sketched. Starting from a standard VCSEL structure Figure 6.14.a, the first grating (that from now on will be named as **bottom grating**), in Figure 6.14.b, can be obtained by coating the outcoupling facet with a certain resist (usually a thermoplastic or UV-curable polymer) capable to be deformed and impressing on it a mold, previously obtained by means of advanced lithographic techniques such as electron beam lithography (EBL) or focused ion beam (FIB) with the desired grating pattern. The imprinting process can be performed into two different ways:

- Thermal nano-imprinting (T-NIL) → both the mold and the substrate are heated, then the mold is pressed into the softened resist, causing it to flow and fill the grating pattern in the mold.
- UV nano-imprinting (UV-NIL) → a UV-sensitive resist can be used, so that the imprinting is performed at room temperature, and UV light is used to cure and harden the resist while the mold is in contact with it.

Once the pattern have been transferred, Figure 6.14.c, the mold must be carefully removed, leaving the structure to be free for an additional treatment. From now on, the most crucial steps of the entire structure are going to be explained. Depositing a sufficiently wide thickness of titanium dioxide ( $\text{TiO}_2$ ) Figure 6.14.d, a material technologically compatible with the VCSELs operating principles, and coating it with a resist, the second mold (with a period higher than the first one) can be imprinted Figure 6.14.e, by means of T-NIL technique, letting the sol-gel to flow and completely fill the grating's features 6.14.f. Carefully demolding, the second grating (that from now on will be named as **upper grating**) is correctly created, Figure 6.14.e and the VCSEL realization can proceed as it is usually done, Figure 6.14.h adding the external contacts.

### 6.3 Titanium dioxide $\text{TiO}_2$ sol-gel processes

Referring to the previous section the critical part of the entire process is the definition of the  $\text{TiO}_2$  sol-gel. Chemically speaking, the sol-gel process, is a synthesis method devoted not only to the inorganic polymerization reactions, but also to the synthesis of nanoscopic organic/inorganic hybrid materials through the incorporation of low molecular weight and oligomeric/polymeric organic molecules with appropriate inorganic moieties [37]. The increasing interest on these compounds is linked do their nanoscopic size that aim to enhance their thermal, melting and viscosity properties that ultimately modify their electronic properties. Among the several sol-gel materials available, in this section the attention is focused on  $\text{TiO}_2$ , a photosensitive titanium organic compound.

TiO<sub>2</sub> has received a great deal of attention since it is an high refractive index material and it has been yet used as anti-reflecting coating in solar cells, as thin-film in optical devices; moreover it has been employed in GaN-based VCSEL with TiO<sub>2</sub> high-index-contrast grating [38], [39], gaining lot of interest for possible applications for sub-wavelength gratings.

Let's explain briefly the most important TiO<sub>2</sub> sol-gel properties. The sol-gel process is employed in the synthesis of thin films, powders, and membranes. It can be categorized into two main approaches: the alkoxide and non-alkoxide routes, each resulting in distinct physical and chemical properties. The most employed one is the alkoxide route, a method that lead to the formation of the desired TiO<sub>2</sub> sol-gel starting from titanium alkoxides and exploiting two different strategies:

- **In-Situ approach** → refers to the direct formation of TiO<sub>2</sub> within the matrix or medium where it will be utilized, without the need for transfer from an external location. This approach offers enhanced control over the interaction between TiO<sub>2</sub> and the surrounding material, leading to improved adhesion, stability, and functionality. Typically, a titanium precursor, such as titanium alkoxide, is introduced into the medium, where it undergoes hydrolysis and condensation reactions, resulting in the in situ formation of TiO<sub>2</sub>. This method ensures uniform distribution and strong integration of TiO<sub>2</sub> within the host matrix. It is frequently employed for creating coatings or composites where TiO<sub>2</sub> nanoparticles are embedded, as well as in applications like photocatalysis and sensors, where the TiO<sub>2</sub> serves as a functional component.
- **Ex-situ approach** → Ex situ refers to the formation of TiO<sub>2</sub> in a separate, external environment before being incorporated into its final application. In this approach, TiO<sub>2</sub> is independently synthesized, often in the form of nanoparticles and subsequently added to a host matrix or used as a coating. The synthesis takes place in a controlled environment, frequently employing techniques such as chemical vapor deposition. Once produced, the TiO<sub>2</sub> is isolated, purified, and then integrated into the desired material. This method allows for precise control over key properties, including particle size, crystallinity, and morphology, as the synthesis can be finely tuned. Additionally, it enables pre-characterization and testing of TiO<sub>2</sub> before its final application. Ex-situ TiO<sub>2</sub> is commonly used in pigments, sunscreens, and various photo-catalytic applications, where a well-defined material is essential.

The validity of this technique rises from the fact that it is possible to combine T-NIL and UV-NIL for the nanostructures fabrication: in particular, using the T-NIL at  $T = 300^{\circ}C$  and after UV-exposure the patterned structures can be converted into inorganic oxide by photo-curing thanks to the photoactivity of the TiO<sub>2</sub> network

that locally induce the degradation of organic species. Moreover, among all the potentialities of this material, carefully described in [40] [41] [42] the one that is important for the purpose of this thesis is the tailoring of the refractive index through UV exposure.

Figure 6.15 shows the evolution of the refractive index of the  $\text{TiO}_2$  sol-gel for different temperature treatment for both in-situ and ex-situ approaches (data refer to [40]). In-situ approach shows a slight refractive index growth  $n \in [1.70, 2]$ , while the ex-situ refractive index remains almost constant with thermal treatment. At  $T < 150^\circ\text{C}$ , the organic components are still in both the cases (organic components that can be degraded after an additional thermal exposure of 30 min at  $T = 300^\circ\text{C}$ ), but the densification of in situ sample is more efficient increasing the value of  $n$ . Whereas, even if in the ex situ film, the presence of anatase nanoparticles should further contribute to increasing the film's refractive index, a poor compaction efficiency of the nanoparticles reducing  $n$ .

Suitable and stable values of  $n$  can be achieved after UV exposure followed by a thermal treatment at  $300^\circ\text{C}$ , devoted to the degradation of the organic part, that will lead to an ultimate value of  $n \simeq 2$ . Of course, this value is sensitive to the UV dose, time of exposure, thermal curing, and kind of UV lamp used.

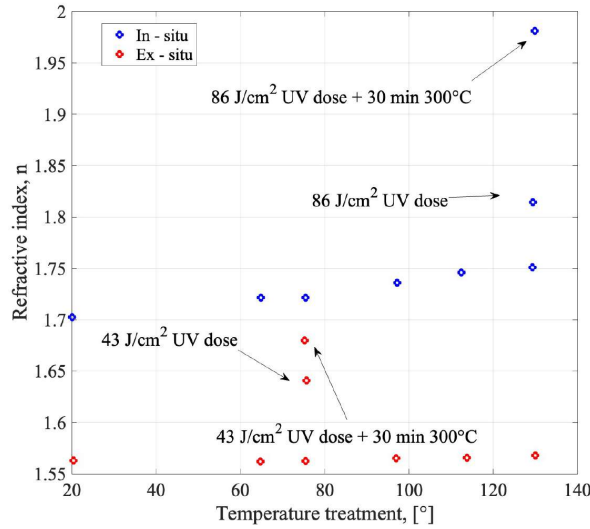


**Figure 6.15:** Refractive index plot in function of the value of the temperature treatment of the sol-gel.

The final choice of what of the two approaches could be used depends on the single case, on the characteristics that the single application accomplish considering a

series of factors that impact (viscosity, porosity, vertical and/or lateral shrinkage, refractive index).

## 6.4 Studies and technological implementations

In figure 6.16 a sketch of the proposed 3D structure is reported. As in standard VCSEL, starting from the bottom and moving to the top, the structure is composed of a substrate, the bottom DBR, the active region, top DBR, bottom grating, spacer and the upper grating.

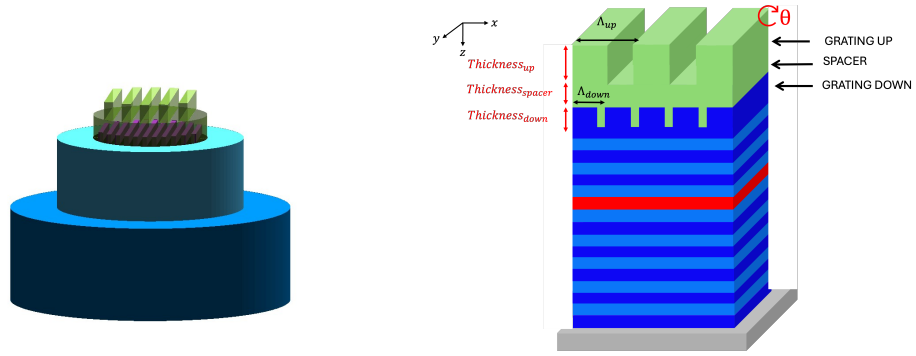


**Figure 6.16:** 3D double-grating VCSEL structure (left); simplified sketch with relevant parameters definition (right).

The simulations' results here reported refer to a 1D structure, where some parameters have been kept fixed for the entire analysis; in particular:

- bottom and top DBR have respectively, 35 and 20 pairs of mirrors;
- the bottom grating has a thickness of 70 nm, it is aligned with respect to the AlGaAs crystalline axes, with a period of  $150\text{nm}$  and  $\eta = 0.5$ ;
- the upper grating has a period equal to the double of the one of the bottom grating and same duty-cycle;
- the spacer and up grating refractive index has been set to a nominal value of  $n = 2$ .

the other parameters may change according to different cases and will be highlighted once per time. The refractive index profile of the structure is reported in 6.17.

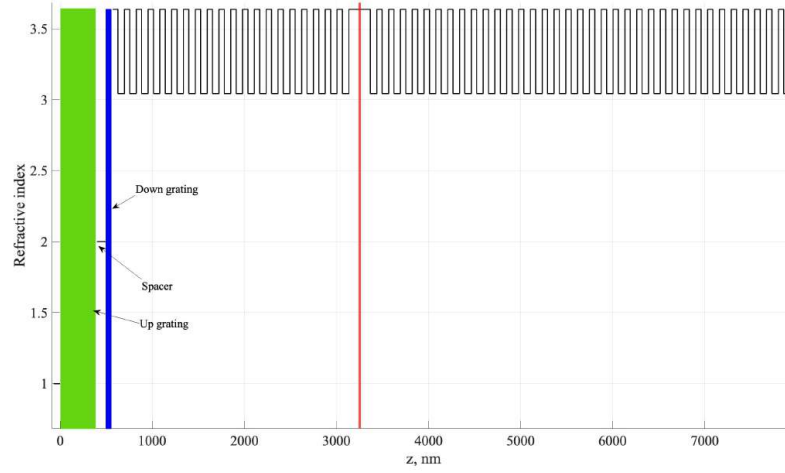


**Figure 6.17:** Refractive index profile of the double-grating 1D-VCSEL structure.

## 6.5 1D modelling results

This section is devoted to the results of the 1D electromagnetic analysis performed on the double-grating VCSEL; the core concept is the identification of an operating range of values for the design of the structure. Different attempts have been performed, changing one the more critical technological parameters. In all the following plot results, the parameter that has been plotted is  $S_3$ ; since  $S_3 \pm 1$  identify CP, black contour lines identify regions where  $S_3 > 0.95$  in order to make more clear the interpretation of the results.

The first attempt is devoted to the understanding of the most suitable rotating angle of the upper grating, able to guarantee the best result in terms of CP. For this analysis technologically coherent parameters have been fixed (to be confirmed in the successive analysis) concerning the spacer thickness at 100 nm; the effects of the VCSEL intrinsic anisotropies, *e.g.* the elasto-optic anisotropy have been treated with a strain value of  $\epsilon = 1 \cdot 10^{-4}$ . As it is reported in Figure 6.18 CP can be achieved by means of  $\theta \in [30, 70]^\circ$  and  $t \in [350, 450]$  nm giving rise to a sufficiently wide operating range both in terms of rotating angle and grating thickness; or for a small interval with  $t \simeq 600$  nm and  $\theta \in [20, 40]^\circ$ . Being the first operating interval more robust, it has been chosen the one to investigate deeply for the subsequent analysis.

Fixing the upper grating rotating angle at  $45^\circ$ , compatible with the previous result, the attention has been pointed on the spacer design. In particular, the previous fixed thickness of the spacer, fixed at 100nm has been investigated. The validity of this value has been confirmed by the parametric analysis, see Figure 6.19 (left), where

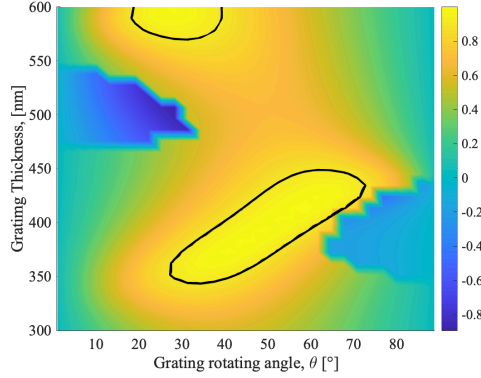


**Figure 6.18:**  $S_3$  map of the lasing mode for different grating rotating angles.

an interesting behaviour is evident. The spacer thickness suitable for CP shows a periodic behaviour, giving rise to a wide range of tolerances by the technological process point of view. This property has been further investigated by fixing the upper grating thickness at  $t = 400$  nm and varying the period  $\Lambda = 200, 300, 400$  nm: in all the cases, see Figure 6.19 (right),  $S_3 = +1$  can be obtained for spacer thickness of 100 nm, 300 nm and so on. In the structure under analysis, no losses sources have been considered that could negatively affect this periodic behaviour. Nevertheless, the spacer thickness has been demonstrated to being fixed at  $\simeq 100$  nm and the previous thickness interval of the upper grating  $t \in [350, 450]$  nm has been confirmed, being a promising result.

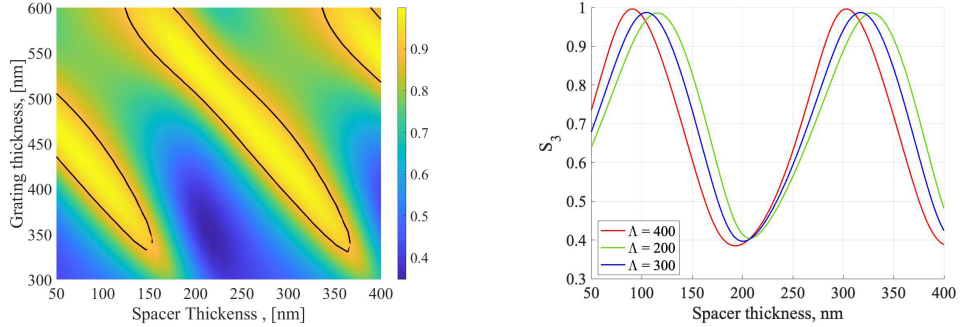


**Figure 6.19:**  $S_3$  map of the lasing mode for different grating periods (right);  $S_3$  comparison plot for  $\Lambda = 200, 300, 400$  nm and different grating thicknesses (left).

The choice of keep fixed the upper grating period as the double of the one of the bottom grating has been chosen as an initial assumption for technological reason linked to process limitation of NIL. Nevertheless, even in this case process variations may be present, thus a parametric variation of  $\Lambda_{up}$  has been performed around the

nominal value of 300 nm, *e.g.*  $\Lambda_{up} \in [200, 400]$  nm. In Figure 6.20 is evident that a grating thickness of  $t \simeq 400$  nm is robust enough for technological tolerances related to the grating period, showing almost a constant behaviour in terms of  $S_3$ .

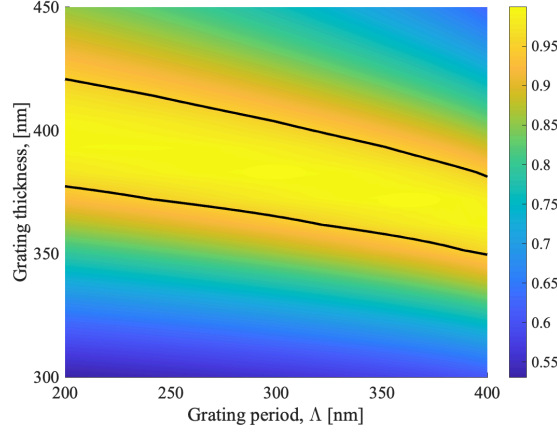


**Figure 6.20:**  $S_3$  lasing mode map for different grating periods and thicknesses.

The robustness of the design has been investigated with respect to the intrinsic anisotropies, here described by means of the elasto-optic effect. The last, is induced by the strain with typical nominal values of  $\epsilon = \pm[1, 2] \cdot 10^{-4}$ . Looking at Figure 6.21 (left) obtained varying the strain values, the grating thickness values achieved in the previous analysis have been confirmed, thus demonstrating the solidity of the design for high values of tensile strain. For compressive strain slightly higher values of grating thicknesses are required but always remaining within the aforementioned values.

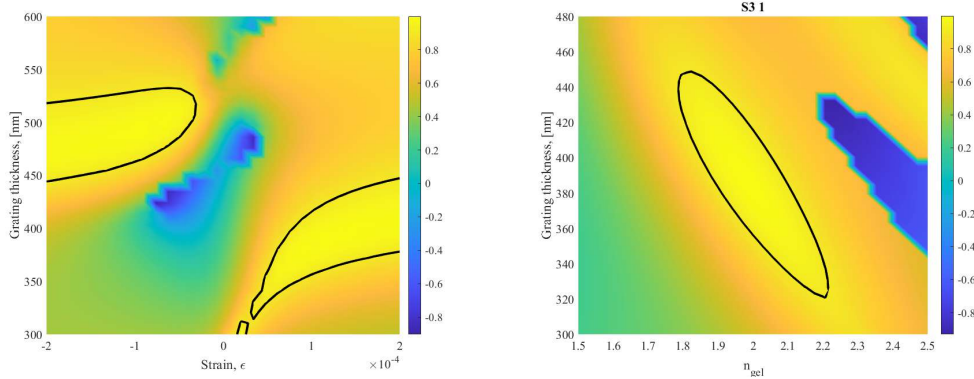


**Figure 6.21:**  $S_3$  lasing mode map for different values of applied strain (left).  $S_3$  map in function of the sol-gel refractive index parametric variation (right).

The most crucial point is the particular sensitivity of the structure to the processes devoted to the definition of the  $\text{TiO}_2$  sol-gel, namely the post-baking and thermal curing steps. This problem will affect all the sol-gel properties and among the others of course the value of the refractive index. This means that the value of  $n$  associated to the grating and to the spacer is not so simple to be determined; thus a parametric variations within the nominal value of  $n = 2$  has been taken into account in order to address this technological issue. The result of the analysis, reported in Figure 6.21 (right), shows that CP can be obtained when  $n \in [1.8, 2.2]$  and for the same values of grating thickness previous discussed.



## Chapter 7

# Final considerations and future works

This research has yielded significant findings that contribute to the ongoing advancements in CP-VCSELs and shed light on the complex interplay between technological process limitation implementations, electromagnetic requirements and application demanding. The grating VCSEL proposed designs integrates all the previous requirements, achieved promising results.

Single grating VCSEL structure, even if easier to be technologically implement, shows CP only in one specific case. Even though it seems to work correctly, the structure is highly sensitive to external tolerances, and what is more, due to the fact that lot of times the elasto- and electro- optic effect are difficult to estimate, an implementation sufficiently independent from these intrinsic anisotropies is required.

The most substantial and robust improvements have been observed in the double-grating design, where wide technological range of validity have been obtained. By modulating the spacer and upper grating thickness, the refractive index of the sol-gel material and finely control the elasto-optic effect in the structure, CP has been achieved in lot of possible configurations. Interestingly, also the single-grating structure may lead to the wanted result, but being less robust it can be promisingly employed for elliptical polarization applications.

These studies suggest that for a complete and deep analysis of the validity of the proposed design, in the case of double-grating structure, a fruitful collaboration with industrial partners, able to properly grow such structures, must be ensured in order to properly define the sol-gel properties, essential for all the electromagnetic analysis and the overall correct working principle of the device. As it is been

demonstrated, technological steps for the definition of the sol-gel processes highly affect the quality of the device components and consequently on the degree of CP. Nevertheless, wide range of tolerances have been obtained in terms of technological limitations, operating range that must be further investigate with deeper analysis considering a complete 3D structure.

Being this work an initial investigation on this double-structure VCSEL, further studies are required in order to investigate more the potentialities of the proposed design, especially in terms of electrical and thermal fields leading to the understanding of additional possible parameters that can negatively influence and may degrade CP.

To conclude, these results show us a certainly promising considerations for future technologically implementations in the view of more compact devices, not requiring external tools for polarization conversion. The emerging applications in terms of P-LIDARs, atomic clocks and atomic magnetometers in particular, may benefit of these studies for a concrete implementation of these new technologies.

# Bibliography

- [1] Kenichi Iga. «VCSELs: Its Concept, Physics, and Development». In: *2021 26th Microoptics Conference (MOC)*. IEEE. 2021, pp. 1–2 (cit. on p. 1).
- [2] Kenichi Iga. «Surface-emitting laser-its birth and generation of new optoelectronics field». In: *IEEE Journal of selected topics in Quantum Electronics* 6.6 (2000), pp. 1201–1215 (cit. on p. 1).
- [3] A. Einstein. *7. Zur Quantentheorie der Strahlung*. pp 209-228. Berlin, Boston: De Gruyter: Quantentheorie: Einführung und Originaltexte, 1916 (cit. on p. 2).
- [4] Milan L. Mashanovitch Larry A. Scott W. Corzine. *Diode lasers and photonic integrated circuits*. - Vol 218. John Wiley Sons: Coldren, 2012 (cit. on p. 4).
- [5] R. Jambunathan and J. Singh. «Design studies for distributed Bragg reflectors for short-cavity edge-emitting lasers - in IEEE Journal of Quantum Electronics». In: 33, no.7 (1997), pp. 1180–1189 (cit. on p. 4).
- [6] A Mereuta, A Syrbu, V Iakovlev, A Rudra, A Caliman, G Suruceanu, C-A Berseth, E Deichsel, and E Kapon. «1.5  $\mu\text{m}$  VCSELs structure optimization for high-power and high-temperature operation». In: *Journal of Crystal growth* 272.1-4 (2004), pp. 520–525 (cit. on p. 5).
- [7] Nikolay N Ledentsov, O Yu Makarov, Vitaly A Shchukin, VP Kalosha, N Ledentsov, L Chrochos, M Bou Sanayeh, and Jarosław Piotr Turkiewicz. «High speed VCSEL technology and applications». In: *Journal of Lightwave Technology* 40.6 (2022), pp. 1749–1763 (cit. on p. 7).
- [8] Fumio Koyama. «Recent advances of VCSEL photonics». In: *Journal of Lightwave Technology* 24.12 (2006), pp. 4502–4513 (cit. on p. 7).
- [9] Dennis H Goldstein. *Polarized light*. CRC press, 2017 (cit. on p. 7).
- [10] 1944 Nobel Prize Winner Prof. I.I. Rabi. «COSMIC PENDULUM' FOR CLOCK PLANNED; Radio Frequencies in Hearts of Atoms Would Be Used in Most Accurate of Timepieces DESIGN TERMED FEASIBLE». In: *Vertical-Cavity Surface-Emitting Lasers XI*. New York Times. 1944 (cit. on p. 8).

- [11] *Il secondo*. URL: <https://www.inrim.it/it/ricerca/campioni-primari/il-secondo#:~:text=il%20secondo%2C%20il%20cui%20simbolo,%2C%20che%20equivale%20a%20s%E2%80%93> 931 (cit. on p. 8).
- [12] Darwin K Serkland, Kent M Geib, Gregory Merwin Peake, Robert Lutwak, Ahmed Rashed, Mathew Varghese, Gary Tepolt, and Mark Prouty. «VCSELs for atomic sensors». In: *Vertical-Cavity Surface-Emitting Lasers XI*. Vol. 6484. SPIE. 2007, pp. 48–57 (cit. on p. 8).
- [13] John Kitching. «Chip-scale atomic devices». In: *Applied Physics Reviews* 5.3 (2018) (cit. on pp. 8–10).
- [14] Peng Zhou, Wei Quan, Kai Wei, Zihua Liang, Jinsheng Hu, Lu Liu, Gen Hu, Ankang Wang, and Mao Ye. «Application of VCSELs in bio-sensing atomic magnetometers». In: *Biosensors* 12.12 (2022), p. 1098 (cit. on p. 11).
- [15] Yuantian Lu, Tian Zhao, Wanhua Zhu, Leisong Liu, Xin Zhuang, Guangyou Fang, and Xiaojuan Zhang. «Recent progress of atomic magnetometers for geomagnetic applications». In: *Sensors* 23.11 (2023), p. 5318 (cit. on p. 11).
- [16] Yi-Yang Xie et al. «Metasurface-integrated vertical cavity surface-emitting lasers for programmable directional lasing emissions». In: *Nature nanotechnology* 15.2 (2020), pp. 125–130 (cit. on p. 12).
- [17] Alberto Tibaldi, Francesco Bertazzi, Michele Goano, Rainer Michalzik, and Pierluigi Debernardi. «VENUS: A Vertical-Cavity Surface-Emitting Laser Electro-Opto-Thermal NUMERICAL Simulator». In: *IEEE Journal of Selected Topics in Quantum Electronics* 25.6 (2019), pp. 1–12. DOI: 10.1109/JSTQE.2019.2893755 (cit. on p. 13).
- [18] Wei-Ping Huang. «Coupled-mode theory for optical waveguides: an overview». In: *JOSA A* 11.3 (1994), pp. 963–983 (cit. on p. 13).
- [19] Pierluigi Debernardi and Gian Paolo Bava. «Coupled mode theory: a powerful tool for analyzing complex VCSELs and designing advanced device features». In: *IEEE Journal of selected topics in quantum electronics* 9.3 (2003), pp. 905–917 (cit. on p. 14).
- [20] P Debernardi and GP Bava. «Effects of Anisotropies on Vectorial Modes of Vertical-Cavity Surface-Emitting Lasers». In: *physica status solidi (a)* 188.3 (2001), pp. 967–977 (cit. on pp. 21, 46).
- [21] J.M. Ostermann, P. Debernardi, and R. Michalzik. «Optimized integrated surface grating design for polarization-stable VCSELs». In: *IEEE Journal of Quantum Electronics* 42.7 (2006), pp. 690–698. DOI: 10.1109/JQE.2006.876721 (cit. on pp. 21, 30).

- [22] Johannes Michael Ostermann, Pierluigi Debernardi, Christof Jalics, Andrea Kroner, Michael C Riedl, and Rainer Michalzik. «Surface gratings for polarization control of single-and multi-mode oxide-confined vertical-cavity surface-emitting lasers». In: *Optics Communications* 246.4-6 (2005), pp. 511–519 (cit. on pp. 21, 30).
- [23] Pierluigi Debernardi, Johannes Michael Ostermann, Martin Feneberg, Christof Jalics, and Rainer Michalzik. «Reliable polarization control of VCSELs through monolithically integrated surface gratings: a comparative theoretical and experimental study». In: *IEEE Journal of selected topics in quantum electronics* 11.1 (2005), pp. 107–116 (cit. on pp. 21, 30).
- [24] Max Born and Emil Wolf. *Principles of optics: electromagnetic theory of propagation, interference and diffraction of light*. Elsevier, 2013 (cit. on pp. 25, 28, 29).
- [25] F Bryant. «Snell’s law of refraction». In: *Physics Bulletin* 9.12 (1958), p. 317 (cit. on p. 26).
- [26] Mitsuaki Shimizu, Fumio Koyama, and Kenichi Iga. «Polarization characteristics of MOCVD grown GaAs/GaAlAs CBH surface emitting lasers». In: *Integrated and Guided Wave Optics*. Optica Publishing Group. 1988, WA3 (cit. on p. 29).
- [27] MG Moharam, Eric B Grann, Drew A Pommet, and TK Gaylord. «Formulation for stable and efficient implementation of the rigorous coupled-wave analysis of binary gratings». In: *JOSA a* 12.5 (1995), pp. 1068–1076 (cit. on p. 31).
- [28] Xiuqin Zhan, Fa-Feng Xu, Zhonghao Zhou, Yongli Yan, Jiannian Yao, and Yong Sheng Zhao. «3D laser displays based on circularly polarized lasing from cholesteric liquid crystal arrays». In: *Advanced Materials* 33.37 (2021), p. 2104418 (cit. on p. 36).
- [29] YiMing Zhu, Fan Zhang, Jie Liu, John D Zhang, Akhlesh Lakhtakia, Jian Xu, et al. «Stable circularly polarized emission from a vertical-cavity surface-emitting laser with a chiral reflector». In: *Applied Physics Express* 5.3 (2012), p. 032102 (cit. on pp. 36, 37).
- [30] Xiangli Jia, Jonas Kapraun, Jiaying Wang, Jipeng Qi, Yipeng Ji, and Connie Chang-Hasnain. «Metasurface reflector enables room-temperature circularly polarized emission from VCSELs». In: *Optica* 10.8 (2023), pp. 1093–1099 (cit. on pp. 37, 38).
- [31] Valerio Torrelli, Martino D’Alessandro, Wolfgang Elsässer, and Pierluigi Debernardi. «On-demand polarization by a vertical-cavity surface-emitting laser with two tilted sub-wavelength gratings». In: *Optics Letters* 49.13 (2024), pp. 3773–3776 (cit. on pp. 37, 38).

- [32] Salah Guessoum, Athanasios Kyriazis, Tushar Malica, Jürgen Van Erps, Geert Van Steenberge, and Martin Virte. «Wavelength tuning of VCSELs via controlled strain». In: *Optics Letters* 49.15 (2024), pp. 4477–4480 (cit. on p. 44).
- [33] Merwan Mokhtari, Philippe Pagnod-Rossiaux, Christophe Levallois, Francois Laruelle, Daniel T Cassidy, Mauro Bettati, and Jean-Pierre Landesman. «Mechanical strain mapping of GaAs based VCSELs». In: *Applied Physics Letters* 118.9 (2021) (cit. on p. 44).
- [34] Torrelli, Miri, D’Alessandro, Gullino, de Gennaro, Elsässer, Tibaldi, and Debernardi. «Understanding polarization with gratings tilted to crystal axes: towards circularly-polarized VCSELs». In preparazione. Manuscritto non pubblicato. 2024 (cit. on p. 49).
- [35] Alberto Gullino, Alberto Tibaldi, Francesco Bertazzi, Michele Goano, and Pierluigi Debernardi. «Reduced dimensionality multiphysics model for efficient VCSELs optimization». In: *Applied Sciences* 11.15 (2021), p. 6908 (cit. on p. 50).
- [36] L Jay Guo. «Nanoimprint lithography: methods and material requirements». In: *Advanced materials* 19.4 (2007), pp. 495–513 (cit. on p. 53).
- [37] Jianye Wen and Garth L Wilkes. «Organic/inorganic hybrid network materials by the sol- gel approach». In: *Chemistry of Materials* 8.8 (1996), pp. 1667–1681 (cit. on p. 54).
- [38] Tsu-Chi Chang, Ehsan Hashemi, Kuo-Bin Hong, Jorgen Bengtsson, Johan Gustavsson, Åsa Haglund, and Tien-Chang Lu. «Electrically injected GaN-based vertical-cavity surface-emitting lasers with TiO<sub>2</sub> high-index-contrast grating reflectors». In: *ACS Photonics* 7.4 (2020), pp. 861–866 (cit. on p. 55).
- [39] Ehsan Hashemi, Jörgen Bengtsson, Johan S Gustavsson, Stefan Carlsson, Georg Rossbach, and Åsa Haglund. «TiO<sub>2</sub> membrane high-contrast grating reflectors for vertical-cavity light-emitters in the visible wavelength regime». In: *Journal of Vacuum Science & Technology B* 33.5 (2015) (cit. on p. 55).
- [40] E Zanchetta, G Della Giustina, A Gandin, V Auzelyte, and G Brusatin. «One-step fabrication of high refractive index inorganic nanostructures». In: *Journal Of Sol-Gel Science And Technology* (2021), pp. 1–11 (cit. on p. 56).
- [41] Agnese Virginia Savegnago. «New organic-inorganic sol-gel resists for micro and nanoimprinting». Recuperata da Overleaf. Tesi di Laurea. Università degli studi di Padova, 2012. URL: <https://hdl.handle.net/20.500.12608/14713> (cit. on p. 56).

- [42] Changli Lü and Bai Yang. «High refractive index organic–inorganic nanocomposites: design, synthesis and application». In: *Journal of Materials Chemistry* 19.19 (2009), pp. 2884–2901 (cit. on p. 56).